Neural G0: a quiescent-like state found in neuroepithelial-derived cells and glioma

Heather M. Feldman[1], Chad M. Toledo[1,2], Sonali Arora[1], Pia Hoellerbauer[1,2], Philip Corrin[1], Lucas Carter[1], Megan Kufeld[1], Hamid Bolouri[1], Ryan Basom[3], Jeffrey Delrow[3], Joshua Meier[4], José L. McFaline-Figueroa[5], Cole Trapnell[5], Steven M. Pollard[6], Anoop Patel[7], Christopher L. Plaisier[8]* and Patrick J. Paddison[1,2]*

[1]Human Biology Division, Fred Hutchinson Cancer Research Center, Seattle, WA 98109; [2]Molecular and Cellular Biology Program, University of Washington, Seattle, WA 98195; [3]Genomics and Bioinformatics Shared Resources, Fred Hutchinson Cancer Research Center, Seattle, WA 98109;[4]Department of Brain and Cognitive Sciences and Biological Engineering, MIT; [5]Department of Genome Sciences, University of Washington, Seattle, WA 98195; [6]Edinburgh CRUK Cancer Research Centre and MRC Centre for Regenerative Medicine, The University of Edinburgh, Edinburgh, UK EH16 4UU; [7]Department of Neurosurgery, University of Washington, Seattle, WA 98195; [8]School of Biological and Health Systems Engineering, Arizona State University, Tempe, AZ 85281.

*To whom correspondence should be addressed: Christopher Plaisier (plaisier@asu.edu) or Patrick Paddison (paddison@fredhutch.org).

Abstract

In depth knowledge of the cellular states associated with normal and disease tissue homeostasis is critical for understanding disease etiology and uncovering therapeutic opportunities. Here, we used single cell RNA-seq to survey the cellular states of neuroepithelial-derived cells in cortical and neurogenic regions of developing and adult mammalian brain to compare with 38,474 cells obtained from 59 human gliomas, as well as pluripotent ESCs, endothelial cells, CD45+ immune cells, and non-CNS cancers. This analysis suggests that a significant portion of neuroepithelial-derived stem and progenitor cells and glioma cells that are not in G2/M or S phase exist in two states: G1 or Neural G0, defined by expression of certain neuro-developmental genes. In gliomas, higher overall Neural G0 gene expression is significantly associated with less aggressive gliomas, *IDH1* mutation, and extended patient survival, while also anti-correlated with cell cycle gene expression. Knockout of genes associated with the Hippo/Yap and p53 pathways diminished Neural G0 *in vitro*, resulting in faster G1 transit, down regulation of quiescence-associated markers, and loss of Neural G0 gene expression. Thus, Neural G0 is a dynamic cellular state required for indolent cell cycles in neural-specified stem and progenitors poised for cell division. As a result, Neural G0 occupancy may be an important determinant of glioma tumor progression.

Key words: neural stem cells, glioma, glioblastoma, G0, Quiescence, scRNA-seq, Hippo-YAP pathway, p53, *CREBBP*, *NF2*, *PTPN14*, *TAOK1*, *TP53*, CRISPR-Cas9, functional genomics.

INTRODUCTION (63,000 including spaces)

Most developing and adult tissues are hierarchically organized such that tissue growth and maintenance is driven by the production of lineage-committed cells from populations of tissue-resident stem and progenitor cells (Reya et al. 2001). In adult tissues, stem cells are typically found in a quiescent or reversible G0 state and must re-enter the cell cycle and divide to promote lineage commitment (Doetsch 2003; Obernier et al. 2018). Their progeny, e.g., amplifying progenitors, further balance lineage commitment with proliferation to produce adequate numbers of lineage committed and terminally differentiated cells to keep pace with demand (Lin 2008). While much is known about specific regulatory events governing organismal development and tissue homeostasis, our understanding the cellular states underlying normal remains limited. This includes lack of a detailed picture of how cells enter, maintain, and exit quiescent-like states.

Moreover, many of the underlying mechanisms of human disease can be attributed, in one way or another, to disturbances in stem and progenitor cell compartments. For example, many cancers develop in maligned developmental hierarchies in which cancer stem-like cells give rise to proliferative progeny that comprise the bulk of the cancer (Dirks 2008). A more in-depth understanding of both normal and disease-associated cellular states could provide critical insight into disease etiology and new therapeutic possibilities.

Among the model systems for stem cell biology are neural stem cells (NSCs) derived from the developing mammalian telencephalon (Davis and Temple 1994; Johe et al. 1996). NSCs can be cultured *ex vivo* yet recapitulate the expansion, specification,

and maturation of each of the major cell types in the mammalian central nervous system (Pollard et al. 2006; Sun et al. 2008). We have previously used hNSCs as non-transformed, tissue-appropriate controls for functional genomic screens in patient derived glioblastoma stem-like cells (GSCs) (Danovi et al. 2013; Ding et al. 2013; Hubert et al. 2013; Toledo et al. 2014; Toledo et al. 2015; Ding et al. 2017). We have observed that when GSCs and NSCs are grown in the same *ex vivo* conditions, NCSs have longer doubling times of 40-50hrs compared to 30-40hrs for GSCs isolates. This discrepancy arises from differences in G0/G1 transit times. In NSCs, but not GSCs, G0/G1 transit times are dynamic and variable (e.g., ranging from 4-95hrs). However, passage through the rest of the cell cycle is short and uniform, similar to GSCs (e.g., ~12 hrs for progression through S, G2, and M (see below)). This suggests that NSCs adopt different cellular states during G0/G1, compared to GSCs, perhaps representing a fundamental difference in their underlying cell cycle regulation.

To further investigate NSC-specific G0/G1 states, below, we employed single-cell RNA sequencing (scRNA-seq) analysis to create a gene expression-based phase classifier for their cell cycle (e.g. G1, G2, M, etc.). We then applied this classifier across neuroepithelial and non-neuroepithelial-derived cells and cancers. We then performed functional genomic screens to identify modulators of a novel G0-like state observed in neuroepithelial-derived cells, Neural G0. We find that Neural G0 is a dynamic state that is rate-limiting for the cell cycle, which arises during neural specification and persists through fetal and adult neurogenesis and gliomagenesis.

RESULTS

Identification of cell cycle phases and candidate G0 and G1 subpopulations in human NSCs

ScRNA-seq has recently emerged as a powerful tool to resolve heterogeneous populations of cells as well as cell cycle phases (Macosko et al. 2015; Zheng et al. 2017). To identify cellular gene expression states and specifically G0/G1 subpopulations in hNSCs, we performed scRNA-seq on U5-NSCs cultured cells (Bressan et al. 2017a) either using bulk cultured cells or subpopulations of phenotypically defined G0/G1 cells (Fig. 1A). To accomplish the latter, we sorted for a Cdt1^{+}NSC populations using a stably expressed mCherry gene fused to the ubiquitylation domains of human Cdt1 (Sakaue-Sawano et al. 2008). When cells are in G1 or G0, mCherry-Cdt is stable and readily observable via FACS. However, when cells are in S, G2, or M the fusion protein is potently destabilized the SCF-Skp2 ubiquitin ligase complex. The fidelity of the reporter was confirmed by treatment of cells with HDAC inhibitors which arrest cells in G0/G1.

In total, we performed scRNA-seq on 5973 unsorted and 4562 mCherry-Cdt1^{+} sorted cells from actively dividing U5-NSC cultures (Methods). For the unsorted populations, we then performed unbiased cluster analysis and identified seven prominent clusters each defined by a set of transcriptionally enriched and depleted genes (Fig. 1B; Supplemental Fig. S1A; Supplemental Table S1). We categorized the clusters by examining: cell cycle gene expression hallmarks, gene set enrichment, cluster network analysis, scRNA-seq from G0/G1 sorted populations (Figs. 1B-E). We defined the clusters as follows: Neural G0 (17.3% of cells), G1 (36.7%), Late G1 (6.4%), S (7.2%), S/G2 (10.9%), G2/M (10.6%), and M/early G1 (8.4%) (Fig. 1B). Importantly,

the G0/G1 subpopulations were enriched in the Cdt+ scRNA-seq populations, while late G1, S, S/G2, and G2/M were all significantly depleted (Supplemental Fig. S1A).

The S, S/G2, and G2/M clusters were enriched for genes whose expression peaks in these phases (Cyclebase (Santos et al. 2015)) including *CCNE2* in S-phase and *CCNB1/2* in G2/M (Figs. 1E & F) and produced tightly interconnected networks of key cell cycle genes (Supplemental Fig. S2). This enrichment included the DNA replication genes *PCNA, MCM3/4/5/6/7/10, GMNN, and RPA2/3* for S-phase and the mitosis genes *CDC20*, *AURKA*, and *BUB1* during G2/M (Figs. 1E & F).

There were four definable G0/G1 clusters: G1, M/Early G1, Late G1 and Neural G0. Despite being the largest cluster, the "G1" cluster had the smallest number of enriched genes, which included IGFR1 signaling genes (e.g., *IGFBP3* and *IGFBP5*), and significant reductions of genes expressed in S, S/G2, and G2/M clusters (Figs. 1E & S1C). The M/early G1 cluster showed low but significant residual expression of M phase genes and enrichment for splicing factor genes, which could represent residual mRNA from G2/M (Figs. 1E, S1C, & S2). The Late G1 cluster was defined by genes important in G1 cell cycle progression, including *CCND1* and *MYC*, and enriched for cholesterol biosynthesis, cell adhesion genes, and the subset of YAP target genes, such as *CTGF* and *SERPINE1* (Figs. 1E, S1B, S1C, & S2).

Finally, the Neural G0 cluster also showed significant repression of 246 genes peaking in other phases of cell cycle, including suppression of *CCND1* expression, which is an indicator of cell cycle exit (Sherr 1995) and other cell cycle regulated genes such as *AURKB*, *CCNB1/2*, *CDC20*, *CDK1*, and *MKI67* (Figs. 1E & S1C). Moreover, the 158 up regulated genes defining this cluster were key genes with roles in neural

development, including glial cell differentiation, neurogenesis, neuron differentiation, and oligodendrocyte differentiation (Figs. 1E, S1C, & S2; Supplemental Table SS). These genes included transcription factors with known roles in balancing stem cell identity and differentiation, including *BEX1, HEY1*, *HOPX*, *OLIG2, SOX2, SOX4*, and *SOX9* (Sakamoto et al. 2003; Bergsland et al. 2006; Scott et al. 2010) (Figs. 1E & S2).

Network analysis of mean cluster gene expression resolved the trajectories of cells through the seven clusters into a pattern that fits well with cell cycle progression and predicted transit through G0/G1 (Figs. 1D & S2). Cells from the candidate G0 population were linked solely to the G1 cluster, which is consistent with G0 as a cell cycle exit from G1. The linkages between the clusters are not directed and thus the flow cells may pass in either direction. However, the model is consistent with results below in which we show, that cultured hNSCs enter G0-like state of variable length between M and S-phase. Importantly, this model of cell cycle progression was further validated by unique molecular identify (UMI) counts across clusters, where the counts start low in Neural G0 and peak in G2/M (Supplemental Fig. S1D). UMI counts can be viewed as an approximation of total mRNA expression in scRNA-seq data. Total mRNA expression during the cell cycle exactly follows this pattern, peaking with expression of Cyclin B and other mitotic genes.

Neural G0 is enriched in neuroepithelial-derived stem and progenitor cell populations.

Comparison of our scRNA-seq cell clusters to gene expression profiles derived from *in vivo* neurogenesis samples supported our definition of the Neural G0 cluster. In two independent scRNA-seq analyses of adult rodent neurogenesis (Llorens-Bobadilla et al. 2015; Artegiani et al. 2017), the Neural G0 cluster showed most significant enrichment for genes defining quiescent neural stem cells and oligodendrocyte progenitor cells (Figs. 2A-D). These genes include, among others: *CLU*, *HOPX*, *ID3*, *OLIG2, PTN*, *SYT11*, *S100B*, *SOX9*, *PTPRZ1*, and *TTYH1* (Fig. 2B). Interestingly, for our S, S/G2, G2/M, and M/early G1 cluster genes, we found significant overlap with the activated NSCs of Llorens-Bobadilla et al. (2015) and the NPCs of Artegiani et al. (2017), which are no longer quiescent (Figs. 2C and 2D).

Moreover, analysis of scRNA-seq of mouse embryonic stem cells (mESCs), representing blastocyst-stage pluripotent cells (i.e., pre-neuroepithelial cell), lacked cells from the Neural G0 subpopulation. For this analysis, we used scRNA-seq data from mESCs that were live sorted for DNA content via Hoechst staining into G1, S-phase, and G2/M populations (Buettner et al. 2015). We found that our G1 category captured 83% of their Hoechst G1 cells, our G2/M category captured 89% of their G2/M, and their S-phase cells were split between G1, S, and G2/M, which is consistent with their Hoechst S-phase gate overlapping portions of these populations (Supplemental Fig. S3A). However, the mESCs failed to classify into our Neural G0, Late G1, or M/early G1 categories. This is consistent with the shorter G1 of ESCs compared to somatic cells (Coronado et al. 2013).

To further investigate how Neural G0 might arise during mammalian development, we applied our hNSC cell cycle classifier to the developing human

telencephalon. We analyzed scRNA-seq data from microdissected developing human cerebral cortex samples (PCW 5.85-19), which was previously used to analyze the spatial and temporal developmental trajectories for 11 cell types: astrocytes, oligodendrocyte precursor cells (OPC), microglia, radial glia (RG), intermediate progenitor cells, excitatory cortical neurons, ventral medial ganglionic eminence progenitors, inhibitory cortical interneurons, choroid plexus cells, mural cells, and endothelial cells (Nowakowski et al. 2017). We classified each single cell using our cell cycle categories and cross tabulated with the 11 cell types (Fig. 2E).

We found that the Neural G0 category was significantly enriched in non-dividing astrocytes, OPCs, and RGs (ventral, outer, and truncated), which had a Neural G0 population ranging from 85-72% (Fig. 2E; Supplemental Table S3). The signature diminishes in differentiating cells where G1 becomes the dominant category classification (Fig. 2E): excitatory cortical neuron lineage which originates from RGs, and the inhibitory cortical interneuron lineage which originate from MGE-RGs. We also observe a small but significant M/Early G1 subpopulation among differentiating cells, suggesting that it likely captures lineage committed cells that have just completed mitosis. Further, populations characterized as dividing (i.e., "div", "div1", or "div2") are highly enriched with S/G2 and/or G2/M classified cells, and Neural G0 and G1 are absent or greatly diminished. Further, microglia, which arise from the embryonic mesoderm rather than neuroectoderm (Ginhoux and Garel 2018), do not classify as harboring Neural G0 cells, but instead are classified as G1 and low-RNA. As we show later the myeloid cells from the tumor core and periphery (Darmanis et al. 2017) classify

as low-RNA which is consistent given that microglia are macrophage like cells that perform an immune function in the brain.

These results support the notion that Neural G0 is a bona fide cellular state associated with non-dividing neural epithelial-derived stem and progenitors as well also astrocytes, which may have progenitor-like properties during development, during fetal and adult neurogenesis.

Neural G0 is a prominent subpopulation in human glioma cells.

Gliomas are tumors of the central nervous system which have a neuroepithelial cell of origin (Chen et al. 2012b; Zong et al. 2015). They contain subpopulations of cells with stem cells-like characteristics that include expression of markers associated with NSCs, OPCs, and astrocytes, which may that may contribute to progression, therapy resistance, and tumor recurrence (Dirks 2008; Zong et al. 2015). Recently, scRNA-seq has been applied to human gliomas of different grades and subtypes to reveal intratumoral cellular heterogeneity (Patel et al. 2014; Tirosh et al. 2016; Darmanis et al. 2017; Venteicher et al. 2017; Filbin et al. 2018; Neftel et al. 2019). To address whether Neural G0 also exists in gliomas, we analyzed scRNA-seq data available for 59 gliomas from these studies (Table 1; Supplemental Table S3).

These tumors represent a broad range of gliomas, including: grades II, III, and IV, IDH1wt and mutant tumors, as well as glioma developmental subclasses (i.e., classical, mesenchymal, and proneural) and tumor types (i.e., astrocytoma, oligodendroglioma, GBM, and pediatric diffuse midline gliomas). Our analysis revealed that Neural G0 and G1 are the two most prominent tumor subpopulations regardless of

stage (Table 1; Table S3). The Neural G0 and G1 represent 95.5% and 2.6%, respectively, of stage II oligodendrogliomas, 76% and 16.4% of stage III astrocytomas, 31-39% and 31-56% of stage IV GBMs, and 73.4% and 16.5% of diffuse midline gliomas (Table 1). Developmental subtype analysis of each tumor cell further revealed that Neural G0 subpopulations showed strong bias against appearing in mesenchymal cell subpopulations in stage III and IV cancers. Overall the prevalence of the Neural G0 state diminished as stage increased regardless of subtype (Table 1; Table S3).

Examining non-tumor brain cells types associated with stromal tissue available from Darminis et al., showed that Neural G0 populations could only be found in neuro-epithelial derived cells such as astrocytes, OPCs, and oligodendrocytes, whereas CD45+ cells and endothelial cells were negative. This was further evidenced by analysis of scRNA-seq data from 21 primary and metastatic head and neck cancers (Puram et al. 2017), where we observe that 80.3% of these tumor cells appeared in G1 but none contain a Neural G0 classified cell (Table 1).

Examination of scRNA-seq data for specific Neural G0 genes expressed in glioma revealed that 121 Neural G0 genes were significantly enriched in at least one data set (Supplemental Table S4). 12 genes, in particular, showed the stronges intersection between data sets (Supplemental Table S4; Supplemental Fig S3B), including *EDNRB*, *FABP7*, *GPM6A*, *GMP6B*, *HEY1*, *PRDX1*, *PTPRZ1*, *SCD5*, and *TTYH1*. Interestingly, these genes are preferentially expressed in GBM and LGGs compared to other cancers (Supplemental Fig. S4). Many have known or proposed roles in maintaining NSC/GSC "stemness" (*EDNRB* (Liu et al. 2011), *PTPRZ1* (Fujikawa et al. 2017), *TTYH1* (Kim et al. 2018; Wu et al. 2019)), slow cycling GBM cells

(*FABP7* (Hoang-Minh et al. 2018)), possible neurogenic niche functions (e.g., *GMP6B* (Choi et al. 2013)), and neuroinflammation (*PRDX1* (Kim et al. 2013) and *PTN* (Fernandez-Calle et al. 2017)).

We next determined whether the Neural G0 gene expression would be associated with bulk gene expression, genetic drivers, and survival data from 681 gliomas available in The Cancer Genome Atlas (TCGA; including both GBM and LGG). First, we calculated eigengenes for Neural G0 genes and cell cycle genes (GO BP term Mitotic Cell Cycle = GO:0000278) that could be associated with the genetic drivers and patient survival. An eigengene represents the common variation across each patient tumor, i.e. first principal component corrected for direction if necessary. Figures 3A and 3B show that the Neural G0 eigengene is significantly down regulated as tumor grade increases. Neural G0 eigengene expression is significantly anti-correlated ($R = -0.58$, p-value $< 2.2 \times 10^{-16}$) with cell cycle eigengene expression. Moreover, there is a striking anticorrelation between the Neural G0 and cell cycle eigengenes across tumors, suggesting that the states are mutually exclusive (Fig. 3B).

To examine survival differences, we compared survival of patients with tumors exhibiting higher (top 25%) or lower (bottom 25%) Neural G0 gene expression (Figs. 3C and 3D). This analysis revealed a highly significant trend that tumors with higher Neural G0 expression survive on average 4.6 years longer than low Neural G0 expressing tumors (Fig. 3D). This difference likely driven by grade enrichment, where high Neural G0 tumors are exclusively grade II and III in the TCGA data set, while low tumors are mainly grade IV (Fig 3C), which have much worse survival (Stupp et al. 2005; Claus et al. 2015). Consistent with this notion, Neural G0 signature is also significantly

associated with IDH1/2 mutation (Supplemental Fig. S5), which are primarily found in lower grade glioma (Yan et al. 2009; Claus et al. 2015). However, in a multivariate survival model the Neural G0 eigengene remains a significant predictor of overall survival even with the inclusion of the covariates (tumor grade and IDH1/2 mutation status), suggesting that the Neural G0 cell state is associated with patient survival variance independently from the common glioma survival associated covariates (tumor grade, IDH1/2).

Taken together, these results demonstrate that Neural G0 cells represent significant subpopulations in gliomas, which diminish by grade and are associated with better clinical outcomes. Thus, the results are consistent with a model whereby higher steady-state Neural G0 populations removes cells from the pool of cycling cells leading to slower tumor growth.

CRISPR-Cas9 gene knockout screens identify regulators of Neural G0 *in vitro*.

We next wished to investigate whether the Neural G0 state causes slower cell cycles. To this end, we performed CRISPR-Cas9 screens in hNSCs for genes that when mutated caused a diminished Neural G0. We reasoned that if Neural G0 ingress/egress is rate limiting for NSC cell cycles, diminishing Neural G0 would cause NSCs to cycle faster. If true, a simple pooled LV-sgRNA library outgrowth screen in normal culture conditions should reveal overrepresented sgRNAs that cause diminished Neural G0 (Fig. 4A).

We performed four separate CRISPR-Cas9 outgrowth screens, using three separate libraries, two different time points (10 days versus ~3 weeks), and two different

human NSC isolates, CB660 and U5 (Pollard et al. 2006; Bressan et al. 2017b) (Figs. 4A, 4B, & S5; Supplemental Table S5). These screens revealed dozens of candidate screen hits significantly enriched at the end of outgrowth period (Fig 4B). These sgRNAs targeted genes found mutated across 35 different cancer (Fig. 5C) and validated tumor suppressor genes (Futreal et al. 2004) (Fig. 5D). Examining the intersection of all of our screen data revealed five reproducible and robust proliferation-enhancing screen hits: *CREBBP*, *NF2*, *PTPN14*, *TAOK1*, and *TP53* (Fig. 4C & S5B), which we chose to validate further.

To control for off-target effects, sgRNA tiling screens for each of these genes were performed, whereby each gene was targeted with 138 to 466 sgRNAs tiled across most exons in NSCs during another outgrowth period and again resolved by sgRNA-seq. At least 70% of tiling sgRNAs for each candidate proliferation limiting gene were significantly enriched in NSCs (Supplemental Fig. S6A; Supplemental Table S5), whereas an sgRNA tiled gene essential for DNA replication, *MCM2*, showed significant depletion over time (Fig. 2a) and control, non-targeting (NTC) sgRNAs were largely inert. KO of target genes was confirmed by Western blots (Supplemental Fig. S6B).

KO of *CREBBP, NF2, PTPN14, TAOK1,* and *TP53* in hNSCs caused a significant proliferative advantage over control cells in a 23-day outgrowth competition assay, while KO of the essential gene *KIF11* showed the opposite result (Fig. 4D). However, the competitive advantage did not appear to be based on differences in survival since no changes in Annexin-V staining were observed following normal culturing or in co-cultures, where apoptosis remained <2% regardless of the experimental condition (data not shown).

Using cell proliferation assays (Supplemental Fig. S6C-E), we found that each KO significantly increased cell accumulation in 48-96 hour outgrowth assays. Importantly, this effect was independent of cell density, as KO cells showed increased proliferation at both low and high densities (Supplemental Fig. S6C). Further, the doubling time significantly decreased for each KO, shortening from ~50 hours to 30-40 hours (Fig. 4E), similar to two GSC isolates used in the same assay.

A transient G0-like state is skipped after KO of *CREBBP*, *NF2*, *PTPN14*, *TAOK1*, or *TP53* in NSCs

In order to further investigate changes in cell cycle dynamics, we utilized the fluorescent ubiquitination cell cycle indicator (FUCCI) system (Sakaue-Sawano et al. 2008). In normal culture conditions, ~63% of U5-NSCs cells are in G0/G1, ~15% are in S/G2/M, and the remainder are transitioning between these phases (Fig. 5A). KO of *CREBBP*, *NF2*, *PTPN14*, *TAOK1*, or *TP53*, however, caused a dramatic loss of the G0/G1 populations (reducing the frequency to 47-38%) and significantly lowered the ratio of G0/G1 to S/G2/M cells (~2-4 fold lower) (Fig. 5B,C).

We also measured transit time through G0/G1 and S/G2/M in individual NSCs using time-lapse microscopy (Figs. 5D & S7). For G0/G1 transit times, we found that our control hNSCs exhibit variable G1 transit times and a wide distribution of G0/G1 transit times in control hNSCs, from fast (4.3 hrs), medium, and extremely slow (95 hrs) (averaging 32.5 hrs) (Fig. 5D). By contrast, S/G2/M transit times were much more uniform (~12.4 hrs) (Fig. 5D). KO of *CREBBP*, *NF2*, *PTPN14*, *TAOK1*, or *TP53* dramatically collapsed the distributed G0/G1 transit times leading to a highly significant,

faster transit of <11.7 hrs in KOs ($p<0.0001$) (Figs. 5D & S7). However, S/G2/M transit times were not significantly affected. GSCs also exhibit collapsed and faster G0/G1 transit times, similar to the KO hNSCs (Fig. 5D).

To further examine possible changes in G0/G1 dynamics, we examined molecular features associated with G0, G1, and late G1 (Supplemental Fig. S9A), including Rb phosphorylation, CDK2 activity, and p27 accumulation. In mammals, cell cycle ingress is governed by progressive phosphorylation of Rb by CDK4/6 and CDK2 as cells pass through the restriction point in late G1, causing de-repression of E2F transcription factors (Weinberg 1995; Zetterberg et al. 1995; Sherr and McCormick 2002a; Sherr and McCormick 2002b; Yao et al. 2008). We observed that KO of *CREBBP*, *NF2*, *PTPN14*, *TAOK1*, or *TP53* in U5-NSCs results in a pronounced increase in the intensity of phosphorylated Rb during G1, consistent with an enrichment for a late G1 state.

CDK2 activity correlates with cell cycle progression; if CDK2 activity levels are low during G1, cells enter G0 (Spencer et al. 2013). If CDK2 activity is intermediate (relative to its peak during G2/M), they progress past the restriction point and into S-phase (Spencer et al. 2013). Using the steady-state cytoplasmic to nuclear ratios of a DNA helicase B (DHB)-mVenus reporter as a readout of CDK2 activity (Hahn et al. 2009; Spencer et al. 2013), we observed significant increases in CDK2 activity in each KO in G0/G1 cells (Supplemental Figs. S9C,D). This was true either by total intensity or the proportion of cells with a reporter ratio greater than 1, a ratio which corresponds with the entrance to S-phase observed in mammary epithelium (Spencer et al. 2013).

Control cells averaged ~8% of G1 cells with >1 cytoplasmic:nuclear reporter ratios CDK2 activity, while KOs were 20-27% (Supplemental Fig. S9D).

Another hallmark of G0/quiescence is the stabilization of p27, a G1 cyclin-dependent kinase (CDK) inhibitor required for maintaining G0 (Coats et al. 1996; Susaki et al. 2007). Consistent with loss of transient G0 cells, we observed that KO of *CREBBP*, *NF2*, *PTPN14*, *TAOK1*, or *TP53* resulted in significant reduction of p27 levels in proliferating NSCs (Supplemental Fig. S9E,F).

Collectively, the above data demonstrate that KO of proliferation-limiting genes in U5-NSCs causes a cell autonomous decrease in cell cycle length with less distributed and faster G0/G1 transit times, an increase in the molecular features associated with late G1, and a reduction in the molecular features associated with G0 (Supplemental Fig. S9G). These data are consistent with KOs either blocking entry of cells into a transient G0 state or causing failure to maintain cells in G0. Therefore, we call these G0-skip genes.

G0-skip mutants reprogram G0/G1, diminishing Neural G0 gene expression

To further characterize G0-skip genes, we performed gene expression analysis of KO cells specifically in G0/G1 phase. To this end, RNA-seq was performed on mCherry-CDT1+ sorted NSCs after KO, which captures both G0 and G1 subpopulations (Fig. 6A and Supplemental Table S6). In control NSCs, as expected, comparing G0/G1 sorted cells to unsorted populations revealed down-regulation of genes involved in cell cycle regulation, DNA replication, and mitosis (Fig. 6A & Supplemental Table S7). Overall comparisons between the KOs and NTC U5-NSCs showed that KO of *NF2* and

PTPN14 were most similar by unsupervised clustering as well as having the most overall gene changes, while *TAOK1* KO was most similar to the controls (Fig. 6B). However, comparison of the overlapping up- or down-regulated genes showed that *TAOK1* KO up-regulated genes were more similar to *NF2* and *PTPN14* KO than the other KOs (Supplemental Fig. S10A).

We next evaluated whether KO of the G0 skip genes were consistent with previously published and suggested roles in p53 pathway (for *TP53* and *CREBBP*) (Ito et al. 2001; Fischer 2017) or the Hippo-YAP pathway signaling (for *NF2*, *PTPN14*, and *TAOK1*) (Zhang et al. 2010; Lin et al. 2013; Wilson et al. 2014; Plouffe et al. 2016). Evaluating p53 target genes, we found that only *TP53* KO significantly down-regulated the expression of high confidence p53 targets including: *BAX*, *CDKN1A/p21, RRM2B,* and *ZMAT3* (Fischer 2017) (Figs. 6C & S10B). However, none of the other KOs showed inhibition of p53 targets or p53 itself, strongly suggesting that the other G0-skip genes are not acting through p53-dependent transcriptional activity.

Evaluation of 55 conserved HIPPO-YAP pathway transcriptional targets (Cordenonsi et al. 2011) revealed that each KO, except for *CREBBP*, showed significant enrichment for YAP targets with *NF2* KO having increased expression of the largest subset (Figs. 6C, S10C-E). Interestingly, *NF2* KO activated one subset of YAP targets important in the biological process of extracellular matrix (ECM) organization, while *TAOK1* KO activated a different subset of YAP targets important in nuclear chromosome segregation, such as during mitosis (Supplemental Fig. S10C-E). *NF2* and *PTPN14* KO shared the most overlap in YAP target activation, including targets considered universal Hippo-YAP targets (e.g., *CTGF*, *CYR61*, and *SERPINE1*).

We next used our hNSC cell cycle classifier to determine whether genes associated with each phase change in G0/G1 populations in after KO of *CREBBP*, *NF2*, *PTPN14*, *TAOK1*, or *TP53*. We observed that Neural G0 were significantly down regulated in each KO (Fig. 6D & S11A), which included those expressed in quiescent NSCs and others cited above with key roles in neural development (e.g., *CLU*, *HOPX*, *ID3*, *PTN*, *PTPRZ1*, *SOX2*, and *SOX4*) (Supplemental Fig. S11B,C). By contrast, genes from late G1 cluster, including, for example, *CCND1* and *MYC*, were significantly up regulated in each KO, with *TAOK1* KO cells additionally showing increase in cell cycle phases as well (Fig. 6E & S12A). Examination of G0/G1 sorted populations from two GSC isolates (0131-mesenchymal and 0827-proneural) showed similar trends, with suppression of Neural G0 and G1 signature and higher expression of S and G2/M genes (Supplemental Fig. S13).

For NSC KOs, we also performed a more in-depth analysis of transcriptional changes of cell cycle genes and novel gene sets (Supplemental Fig. S14). These included cell cycle genes that could be causal for reprograming G0/G1 dynamics, such as up-regulation of G1 cyclins, E2F1/2 or down-regulation of CDKN1A/p21 and CDKN1B/p27 (Supplemental Fig. S14A). We also noted that for both *NF2* and *PTPN14* KO there was up-regulation of various Hippo-YAP pathway members, including *LATS2*, *TEAD1,* and *YAP1*, suggesting a possible feedback regulation of the pathway unique to *NF2* and *PTPN14* (Supplemental Fig. S14B) TAOK1 KO, in contrast to other KOs, strongly up-regulated >40 key regulators of mitosis (e.g., *AURKA*, *BUB1*, *CCNB1/2*, *CDK1*, *KIF11*, *etc.*), suggesting it may act to inhibit their precocious activation in G0/G1 or expression after completion of mitosis (Supplemental Fig. S14C).

CREBBP KO, uniquely among KOs, caused up-regulation of key nuclear-encoded mitochondrial genes, including members of the NADH dehydrogenase complex, the succinate dehydrogenase complex, and mitochondrial DNA polymerase (Supplemental Fig. S14D), which are direct transcriptional regulatory targets of nuclear respiratory factors 1 and 2 (NRF1 and NRF2) (Kelly and Scarpulla 2004).

Finally, to more directly confirm reprograming of G0/G1 population in a G0-skip mutant, we performed scRNA-seq on G0/G1-sorted hNSCs with KO of *TAOK1* (Supplemental Fig. S15). The steady-state percentage of Neural G0 and, to a lesser degree, G1 cells in *TAOK1* KO cells is significantly diminished from 21.3% to 10.3% and 58.9% to 53.3%, respectively (Supplemental Fig. S15B,C). However, the late G1 population is increased (from 3.0% to 9.8%) as are cells in the M/early G1 (from 7.8% to 15.3%) and G2/M phase (from 1.5% to 4.4%). The expansion of the M/early G1 in *TAOK1* KO cells could explain the increase in mitotic genes observed in the bulk G0/G1 RNA-seq data in *TAOK1* KO cells (Supplemental Fig. S15C), suggesting that TAOK1 helps attenuate expression of mitotic genes from the previous cell cycle.

These results strongly suggest that NSC G0-skip mutants lose a significant fraction of Neural G0 subpopulation and reprogram G1 transcription networks to promote entry into G1-S.

DISCUSSION

Here, we discovered a G0-like cellular state, Neural G0, in hNSCs and other neuroepithelial-derived cell types, which occurs between cytokinesis and G1 and is enriched for neurodevelomental gene expression. Evidence for Neural G0 is as follows.

First, we observed from scRNA-seq analysis of cultured hNSCs a G0/G1 subpopulation distinct from other G1 and cell cycle populations (Fig. 1 and S1), which differentially expresses genes associated with adult quiescent NSCs, non-dividing OPCs, and neural differentiation (Figs. 1E, 2A-D). Second, by applying our hNSC-derived cell cycle classifier to scRNA-seq data from human corticogenesis, we found that Neural G0 is a prominent subpopulation among non-dividing stem and progenitors, including OPCs and radial glial cells, which was diminished and replaced by G1 cells during differentiation (Fig. 2E). Third, analyzing scRNA-seq from human gliomas also revealed that Neural G0 is a significant non-dividing cell population, which is diminished as tumors become more aggressive and replaced by G1 cells (Table I; Fig. 3). Fourth, we observe that Neural G0 can be ablated *in vitro* through genetic manipulation of at least 5 genes in NSCs *in vitro* (*CREBBP*, *NF2*, *PTPN14*, *TAOK1*, or *TP53*), which causes dramatically faster G0/G1 transit times and loss of Neural G0-associated gene expression (Figs. 5 & 6). Finally, Neural G0 appears to be restricted to neuroepithelial-derived cells, as we failed to find evidence for Neural G0 subpopulations in numerous non-neuroeptithelial cell populations (e.g., CD45+ cells). Taken together, these results demonstrate that Neural G0 is a bona fide cell cycle state *in vitro* and *in vivo*, which is rate-limiting for the cell cycle.

However, Neural G0 is not a singular state. That is, Neural G0 cells found in different cell types (i.e., astrocytes, OPCs, RGs, and glioma cells) are not identical or interchangeable. Instead, each Neural G0 cell is enriched for a portion, but not all, of the 158 genes present in the hNSCs' Neural G0, which helps distinguish it from G1 and other cell cycle phases. The happenstance use of cultured, multipotent hNSCs for our

cell classifier likely enabled casting a wide net for identifying other neural populations in G0-like states. Thereby, G0-like states for non-neuroectoderm cells might be identified using an alternative set of developmental markers (e.g., Mesoderm G0).

If Neural G0 represents a neural-specific cell cycle phase, what is its purpose? One possibility is that Neural G0 provides a compartment for maintenance of neurodevelopmental potential. That is, it allows time for reinforcing transcriptional and epigenetic programs associated with neurodevelopment gene expression. Consistent with this possibility, Neural G0 genes are up regulated in quiescent NSCs *in vivo* and diminished during neural differentiation programs during corticogenesis (Fig. 2E) or by KO of G0-skip genes in CDT+ NSCs (Fig. 6). Moreover, multiple Neural G0 genes are significantly enriched in NSCs and glioma Neural G0 cells which are known to help maintain "stemness". For example, HEY1 and TTYH1 (e.g., Fig S3), are both are key players in Notch signaling pathway in NSCs and help maintain the NSC identity *in vivo* (Kim et al. 2018; Than-Trong et al. 2018). PTN and its target PTPRZ1 also may help promote stemness, signaling, and proliferation of neural progenitors and glioma tumor cells (Fujikawa et al. 2016; Zhang et al. 2016; Fujikawa et al. 2017). Moreover, FABP7 expression and activity have been associated with lipid metabolism in slow-cycling GBM tumor cells, proposed to be responsible for tumor recurrence (Hoang-Minh et al. 2018).

However, other functions for Neural G0 could include: time for repair of DNA lesions that persist from the previous cell cycle (Arora et al. 2017; Barr et al. 2017), responses to oxidative stress and mitochondrial maintenance (Mohrin and Chen 2016), regulation of structural RNAs (e.g., rRNAs, tRNAs)(Roche et al. 2017), as well as

immune-modulatory functions (e.g., neuroinflammation). Future studies will be required to address these and other possibilities.

Our results have important implications for glioma biology. First, our classifier provides a method for identifying G0-like subpopulations in glioma tumor cells. While gliomas were among the first tumors dissected by scRNA-seq (Patel et al. 2014) and also for in depth genomic analysis (e.g., TGCA) (TCGA 2008), scRNA-seq analysis and pathological examination of tumor samples has been up till now unable to distinguish G0 from G1 cells. In general, G0/G1 populations are defined by the absence of S, G2, and M markers (e.g., Ki67 expression). However, our analysis suggests that these populations can be readily identified.

Second, our analysis of 59 gliomas provides unique insight into their biology. We show that the proportion of Neural G0 cells in tumors correlates well with grade, patient survival, and proliferative state of gliomas. Outside of providing an important companion diagnostic to existing methods of grading gliomas, this analysis raises questions about the cellular composition of gliomas and the root causes of progression and responses to therapy. For example, our analysis of lower grade gliomas (LGG) suggests that they are effectively "trapped" in Neural G0, where >93% of grade II cells categorized in Neural G0 (Table I). LGGs produce longer survival times (~7yrs) but are nonetheless uniformly fatal after progression to high grade glioma (Claus et al. 2015). This would be consistent with Neural G0 acting as a barrier to progression in low grade gliomas, which is overcome in secondary gliomas. Because the majority of LGGs (~80%) are IDH1/2mut (Yan et al. 2009)(cBioportal), it is conceivable that IDH1/2mut could promote

Neural G0 (e.g., perhaps through an epigenetic mechanism (Xu et al. 2011)) and slower initial tumor growth.

For grade IV glioma (GBM), some studies have attempted to divide tumors up into fast dividing and slow-dividing cells, for example, based on DNA barcoding experiments which demonstrate that the slower dividing populations have higher tumor initiation potential and more robust responses to treatment regimens (Bao et al. 2006; Lan et al. 2017). These slower-dividing cells have been hypothesized to have stem cell-like characteristics that enable regeneration of tumor subpopulations and engender higher capacity for repair of DNA damage (Chen et al. 2012a). It is tempting to speculate that these slower dividing cells are in fact the Neural G0 cells we identify in GBM samples. In this scenario, Neural G0 populations would be enriched for "stem-like" cells required for tumor maintenance and regrowth of higher grade tumors, while G1 populations would include their "differentiated" progeny.

Lastly, we found that KO of five genes, *CREBBP*, *NF2*, *PTPN14*, *TAOK1*, or *TP53*, all known or candidate tumor suppressors associated with the Hippo/Yap and p53 pathways, diminish Neural G0 *in vitro* in hNSCs. Each KO reduced molecular features associated with G0-like states (e.g., hypophosphorylated Rb, low CDK2 activity, and p27 stabilization) and dramatically reduced G0/G1 transit times, speeding up the cell cycle. Moreover, bulk RNA-seq of G0/G1 populations as well as scRNA-seq of KOs confirmed reduction of Neural G0 genes expression and characteristic and gene expression changes associated with the p53 transcriptional network, Hippo-YAP targets, cell cycle gene regulation, and many novel targets and pathways, including those downstream of CREBBP and TAOK1.

Collectively, our data reveals Neural G0 is cellular state shared by multiple neural epithelial-derived stem and progenitor cell types, which likely plays key roles in neurogenesis and glioma tumor development and recurrence.

METHODS

Cell culture

NSC and GSC lines were grown in NeuroCult NS-A basal medium (StemCell Technologies) supplemented with B27 (Thermo Fisher), N2 (2x stock in Advanced DMEM/F-12 (Fisher) with 25 μg/mL insulin (Sigma), 100 μg/mL apo-Transferrin (Sigma), 6 ng/mL progesterone (Sigma), 16 μg/mL putrescine (Sigma), 30 nM sodium selenite (Sigma), and 50 μg/mL bovine serum albumin (Sigma), and EGF and FGF-2 (20ng/mL each) (Peprotech) on laminin (Sigma or Trevigen) coated polystyrene plates and passaged according to previously published protocols(Pollard et al. 2009). Cells were detached from their plates using Accutase (Thermo Fisher). 293T (ATCC) cells were grown in 10% FBS/DMEM (Invitrogen).

CRISPR-Cas9 screening

For large-scale transduction, NSC cells were plated into T225 flasks at an appropriate density such that each replicate had 250-500-fold representation, using the two previously published CRISPR-Cas9 libraries(Shalem et al. 2014; Doench et al. 2016) (Addgene) or a custom synthesized sgRNA library (Twist Biosciences) targeting 1377 genes derived from(Toledo et al. 2015). NSCs and GSCs were infected at MOI <1 for all cell lines. Cells were infected for 48 hours followed by selection with 1-2 μg/mL

(depending on the target cell type) of puromycin for 3 days. Post-selection, a portion of cells were harvested as Day 0 time point. The remaining cells were then passaged in T225 flasks maintaining 250-500-fold representation and cultured for an additional 21-23 days (~10-15 cell doublings) or 10 days. Genomic DNA was extracted using QiaAmp Blood Purification Mini or Midi kit (Qiagen). A two-step PCR procedure was performed to amplify sgRNA sequence. For the first PCR, DNA was extracted from the number of cells equivalent to 250-500-fold representation (screen-dependent) for each replicate (2-4 replicates) and the entire sample was amplified for the guide region. For each sample, ~100 separate PCR reactions (library and representation dependent) were performed with 1 µg genomic DNA in each reaction using Herculase II Fusion DNA Polymerase (Agilent) or Phusion High-Fidelity DNA Polymerase (Thermo Fisher). Afterwards, a set of second PCRs was performed to add on Illumina adaptors and to barcode samples, using 10-20ul of the product from the first PCR. Primer sequences are in Supplemental Table 8. We used a primer set to include both a variable 1-6 bp sequence to increase library complexity and 6 bp Illumina barcodes for multiplexing of different biological samples. The whole amplification was carried out with 12 cycles for the first PCR and 18 cycles for the second PCR to maintain linear amplification. Resulting amplicons from the second PCR were column purified using Monarch PCR & DNA Cleanup Kit (New England Biolabs; NEB) to remove genomic DNA and first round PCR product. Purified products were quantified (Qubit 2.0 Fluorometer; Fisher), mixed, and sequenced using HiSeq 2500 (Illumina). Bowtie was used to align the sequenced reads to the guides(Langmead et al. 2009). The R/Bioconductor package edgeR was used to assess changes across various groups(Robinson et al. 2010). For the tiling library, only guides

that mapped once to the genome and are within the gene's coding region were considered for further analysis.

Raw and mapped data files are available at the Gene Expression Omnibus database (GSE117004).

Individual lentiviral-sgRNA assembly for validation

For retests, individual or pooled sgRNA were cloned into lentiCRISPR v2 plasmid. Briefly, DNA oligonucleotides were synthesized with sgRNA sequence flanked by the following:

5': tatatcttGTGGAAAGGACGAAACACCg

3': gttttagagctaGAAAtagcaagttaa

PCR was then performed with the ArrayF and ArrayR primers (Supplemental Table 8). The PCR product was gel purified using the ZymoClean Gel DNA recovery kit (Zymo Research). Gibson Assembly Master Mix (NEB) was used to clone the PCR product into lentiCRISPR v2 plasmid(Sanjana et al. 2014). The ligated plasmid was then transformed into Stellar Competent cells (Clontech), and streaked onto LB agar plates. The resulting clones were grown up and sequence verified (GeneWiz).

Lentiviral production

For virus production, lentiCRISPR v2 plasmids(Sanjana et al. 2014) were transfected using polyethylenimine (Polysciences) into 293T cells along with psPAX and pMD2.G packaging plasmids (Addgene) to produce lentivirus. To produce lentivirus for the whole-genome CRISPR-Cas9 libraries, 25x150mm plates of 293T cells were seeded at

~15 million cells per plate. Fresh media was added 24 hours later and viral supernatant harvested 24 and 48 hours after that. For screening, virus was concentrated 1000x following ultracentrifugation at 6800*xg* for 20 hours. For validation, lentivirus was used unconcentrated at an MOI<1.

Viability and Proliferation Assays

Cells were infected with lentiviral gene pools containing 3-4 sgRNAs per gene or with lentivirus containing a single sgRNA to the respective gene (Supplemental Table 8). Initial cell density was carefully controlled for in each experiment by counting cells using a Nucleocounter NC-100 (Eppendorf) and cells were always grown in subconfluent conditions. For viability assays, following selection, cells were outgrown for 7-10 days, then harvested, counted, and plated in triplicate onto 96-well plates coated with laminin in dilution format starting at 1,000 cells to 3,750 cells per well (cell density depended on cell isolate and duration of assay). Cells were fed with fresh medium every 3-4 days. After 7-12 days under standard growth conditions, cell proliferative rates were measured using Alamar blue reagent according to manufacturer's instructions (Invitrogen). For analysis, sgRNA-containing samples were normalized to their respective nontargeting control (NTC) samples. For doubling time assays, cells infected with individual sgRNAs or NTC were routinely cultured (split every 3-5 days), and counted at each split (Nucleocounter NC-100; Eppendorf). The overall growth of each well containing an individual sgRNA was calculated and compared to the NTC well. Comparisons between multiple experiments were normalized.

Competition experiment

NSCs were infected with lentiviral gene pools containing 3-4 sgRNAs per gene, puromycin selected, and mixed with NSCs infected with lentiviruses containing turboGFP at an approximate 1:9 ratio, respectively. Cultures were outgrown for 23 to 31 days and flow analysis (FACS Canto; Becton Dickinson) was conducted every 7-8 days for GFP expression. Flow analysis data was analyzed using FlowJo software. For each sample, the GFP- population for each time point was normalized to its respective Day 0 GFP- population and the NTC (competition index).

Time-lapse microscopy

NSCs were infected with lentiviral gene pools containing 3-4 sgRNAs per gene or with individual sgRNAs, puromycin selected, outgrown for >13 days, and plated onto 96-well plates or 24-well plates. Plates were then inserted into the IncuCyte ZOOM (Essen BioScience), which was in an incubator set to normal culture conditions (37° and 5% CO_2), and analyzed with its software. For the cell confluency experiment, phase images were taken every hour for 72 hours. For the FUCCI cell cycle experiment, images were taken every 10-15 minutes for 72-120 hours. Cell cycle transit time for G0/G1 (mCherry-CDT1(aa30-120)+) and S/G2/M (mAG-Geminin(aa1-110)+) was manually scored by three different observers in actively dividing cells (those that could be followed from mitosis to mitosis). Each KO was scored by at least 2 independent observers and consistency between scorers was checked through shared analysis of a standard.

Western blotting

Cells were harvested, washed with PBS, and either immediately lysed or snap-frozen and stored at -80˚C until lysis. Cells were lysed with modified RIPA buffer (150mM NaCl, 50mM Tris, pH 7.5, 2mM $MgCl_2$, 0.1% SDS, 2mM DDT, 0.4% deoxycholate, 0.4% Triton X-100, 1X complete protease inhibitor cocktail (complete Mini EDTA-free, Roche) and 1U/μL benzonase nuclease (Novagen) at room temperature for 15 minutes. Cell lysates were quantified using Pierce 660nm protein assay reagent and proteins were loaded onto SDS-PAGE for western blot. The Trans-Blot Turbo transfer system (Bio-Rad) was used according to the manufacturer's instructions. See Supplemental Table 8 for antibodies and dilutions. An Odyssey infrared imaging system was used to visualize blots (LI-COR) following the manufacturer's instructions.

Flow Cytometry

FUCCI constructs (RIKEN, gift from Dr. Atsushi Miyawaki) were transduced into wild-type U5-NSCs and sorted sequentially for the presence of mCherry-CDT1(aa30-120) and S/G2/M mAG-Geminin(aa1-110) on an FACSAria II (BD). Normal growth was verified post-sorting and then the FUCCI U5-NSCs were transduced with individual sgRNA-Cas9 (4 independent guides per gene) and selected with 1 μg/mL puromycin. Cells were grown out for 21 days with splitting every 3-4 days and maintaining equivalent densities. Cells were counted (Nucleocounter NC-100; Eppendorf) and plated 3 days before analysis on an LSR II (BD). Controls cultured in the same conditions included cells transduced with guides against 3 non-growth limiting genes, including *GNAS1*, and showed equivalent FUCCI ratios. Results were analyzed using FlowJo software.

Immunofluorescence and CDK2 Activity

U5-NSCs were plated on acid-washed glass coverslips (phosphorylated Rb and CDK2 activity) or 96-well imaging plates (differentiation; Corning). They were fixed overnight in 2% paraformaldehyde (USB) at 4˚C, washed with DPBS (with calcium and magnesium) (Fisher), and blocked and permeabilized with 5% goat serum (Millipore), 1% bovine serum albumin (Sigma), and 0.1% triton X-100 (Fisher) in DPBS for 45 minutes at room temperature. Samples were stained with primary antibody diluted in 5% goat serum in DPBS overnight at 4˚C, washed with DPBS, and stained with secondary antibody (diluted 1:200 in 5% goat serum in DPBS) at 37˚C for 45 minutes. See Supplemental Table 8 for antibodies and dilutions. Samples were washed with DPBS, dyed with 100 ng/mL 4',6-diamidino-2-phenylindole (DAPI) diluted in DPBS for 20 minutes at room temperature, and washed with DPBS. Coverslips were preserved using ProLong Gold Antifade Mountant (Fisher) and inverted on glass slides. For differentiation, images were acquired on Nikon Eclipse Ti using NIS-Elements software (Nikon).

Phosphorylated Rb and CDK2 Activity Image Analysis

Cells were transduced with mVenus-DNA helicase B (DHB) (amino acids 994–1087)(Hahn et al. 2009) (gift from Dr. Sabrina Spencer) and the mCherry-*CDT1* FUCCI and sorted on a FACSAria II flow cytometer (BD). Cells were outgrown to ensure normal growth and then transduced with individual sgRNA-Cas9. After >10 days outgrowth, cells were counted and plated, grown for 2 days, and stained for phosphorylated Rb and imaged on a TISSUEFAXS microscope (TissueGnostics), 54 fields per KO or NTC.

Cells were analyzed using CellProfiler (Kamentsky et al. 2011). G0/G1 nuclei were identified by the presence of the *CDT1* FUCCI reporter (25-120 pixel diameter, Global/Otsu thresholding, and distinguishing clumped objects by shape). CDK2 activity was defined by the cytoplasmic to nuclear ratio of the mVenus-DHB reporter, with the cytoplasmic intensity of the DHB reporter defined as the upper quartile intensity of a 2-pixel ring around the CDT1-defined nucleus due to the irregular shape of the U5-NSCs.

p27 reporter

The p27 reporter was constructed after (Oki et al., 2014), using a p27 allele that harbors two amino acid substitutions (F62A and F64A) that block binding to Cyclin/CDK complexes but do not interfere with its cell cycle-dependent proteolysis. This p27K$^-$ allele was fused to mVenus to create p27K$^-$-mVenus. To this end, the p27 allele and mVenus were synthesized as gBlocks (IDT) and cloned via Gibson assembly (NEB) into a modified pGIPz lentiviral expression vector (Open Biosystems). Lentivirally transduced cells were puromycin selected and validated using mCherry-CDT1 FUCCI and HDAC inhibitor treatment (48 hours of 5 μM apicidin (Cayman)) to induce G0/G1 arrest using FACS (LSR II from Becton Dickinson and FlowJo software).

Bulk RNA sequencing expression analysis

For G0/G1 NSC, cells singly positive for mCherry-*CDT1* FUCCI were sorted on a FACSAria II (BD) directly into TRIzol reagent (Life Technologies). For differentiating cells, cells were sparsely plated and cultured with growth medium without EGF or FGF-2 for 7 days before being lysed with TRIzol reagent. For both, 2 replicates per condition

were harvested. RNA was extracted using Direct-zol RNA MiniPrep Plus (Zymo Research). Total RNA integrity was checked and quantified using a 2200 TapeStation (Agilent). RNA-seq libraries were prepared using the KAPA Stranded mRNA-seq Kit with mRNA capture beads (KAPA Biosystems) according to the manufacturer's guidelines. Library size distributions were validated using a 2200 TapeStation (Agilent). Additional library QC, blending of pooled indexed libraries, and cluster optimization was performed using the Qubit 2.0 Fluorometer (Fisher). RNA-seq libraries were pooled and sequencing was performed using an Illumina HiSeq 2500 in Rapid Run mode employing a paired-end, 50 base read length (PE50) sequencing strategy.

Bulk RNA sequencing data analysis

RNA-seq reads were aligned to the UCSC mm10 assembly using Tophat2 (Trapnell et al. 2012) and counted for gene associations against the UCSC genes database with HTSeq (Anders et al. 2015). Differential expression analysis was performed using R/Bioconductor package edgeR (Robinson et al. 2010). Samples for G0/G1 bulk RNA-seq were collected in two batches, so batch-dependent genes were removed before analysis (inter-batch p-value<0.01 by Wilcoxon-Mann-Whitney). To ensure that no genes were eliminated that may be regulated specific to a particular knockout, genes with a CPM variability greater than 2-fold compared to the internal batch control and an expression greater than 1 CPM in at least one sample were retained. Differentially expressed genes (DEG) at the transcription level were found using a statistical cutoff of FDR < 0.05 and visualized using R/Bioconductor package pheatmap. Kolmogorov-Smirnov test were conducted in R using the function ks.test from stats package. Raw

sequencing data and read count per gene data can be accessed at the NCBI Gene Expression Omnibus (GSE117004).

Gene ontology analysis

Gene Ontology (GO)-based enrichment tests were implemented using GOseq (v 1.23.0)(Young et al. 2010), which corrects for gene length bias. Gene lists were also analyzed for pathways using the R/Bioconductor package ReactomePA (v 1.15.4)(Yu and He 2016). Analysis used all genes either up or down-regulated with a FDR<0.05 compared to NTC. GO terms with adjusted P-values<0.05 were considered significantly enriched. Venn diagrams were generated on http://bioinformatics.psb.ugent.be/webtools/Venn/.

Single cell RNA-sequencing Sample Preparation

Single cell RNA-sequencing was performed using 10x Genomics' reagents, instruments, and protocols. Single cell RNA-Seq libraries were prepared using GemCode Single Cell 3' Gel Bead and Library Kit. FUCCI U5-NSCs (both with and without lentiviral TAOK1 KO, >14 days outgrowth) were harvested and half the cells were sorted using the FACSAria II (BD) for cells singly positive for mCherry-CDT1 FUCCI. Sorted cells were kept on ice before suspensions were loaded on a GemCode Single Cell Instrument to generate single cell gel beads in emulsion (GEMs) (target recovery: 2500 cells). GEM-reverse transcription (RT) was performed in a C1000 Touch Thermal cycler (Bio-Rad) and after RT, GEMs were broken and the single strand cDNA cleaned up with DynaBeads (Fisher) and SPRIselect Reagent Kit (Beckman Coulter). cDNA was amplified, cleaned up and sheared to ~200bp using a Covaris M220 system (Covaris).

Indexed sequencing libraries were constructed using the reagents in the GemCode Single Cell 3' Library Kit, following these steps: 1) end repair and A-tailing; 2) adapter ligation; 3) post-ligation cleanup with SPRIselect; and 4) sample index PCR and cleanup. Library size distributions were validated for quality control using a 2200 TapeStation (Agilent). The barcoded sequencing libraries were quantified by a Qubit 2.0 Fluorometer (Fisher) and sequenced using HiSeq 2500 (Illumina) with the following read lengths: 98bp Read1, 14bp I7 Index, 8bp I5 Index and 10bp Read2. Sequencing data can be accessed at the NCBI Gene Expression Omnibus (GSE117004).

scRNA-seq Analysis

CellRanger (10x Genomics) was used to align, quantify, and provide basic quality control metrics for the scRNA-seq data. Using Seurat version 2.2.1, the scRNA-seq data from wild-type U5 cells and sgTAOK1 knock-out cells were merged and analyzed. Both scRNA-seq data were loaded as counts, normalized, and then scaled while taking into account both percent of mitochondria and the number of UMIs per cell as covariates. The union of the top 1,000 most variant genes from each dataset were used in canonical correlation analysis (CCA) to merge the two datasets via alignment of their subspace. We then identified clusters of cells using a shared nearest neighbor (SNN) modularity optimization-based clustering algorithm. Marker genes for each cluster were identified as differentially expressed genes, and the determination of 8 clusters was based on the discovery of strong markers for 6 of the eight clusters (both the G1 and low RNA clusters did not have significantly upregulated marker genes). Identity of clusters was determined primarily through the expression of cyclins and cyclin-

dependent kinases, and secondarily through the function of other marker genes. A tSNE visualization was generated with a perplexity setting of 23.

Network analysis was used to determine the trajectories of cells through the cell cycle. First, the cluster centroids (mean expression for each gene across all the cells from a cluster) were used to compute the Canberra distance measure. In a cycle like a cell cycle, it is expected that on average there would be 2 edges between each cell cycle state. A distance cutoff of 240 led to 2.28 connections per cluster was used to turn the distance matrix into a network (Futreal et al. 2004).

Network analysis of the clusters was performed using the STRING database (Szklarczyk et al. 2017) and visualized using Cytoscape software. Transcription factors were identified according to TFcheckpoint (Chawla et al. 2013).

Hypergeometric Analysis and Representation Factor Calculations

Hypergeometric tests (Johnson et al. 2005) were carried out in R using function phyper (stat.ethz.ch/R-manual/R-devel/library/stats/html/Hypergeometric.html). Gene lists were pre-filtered for the shared genes in each analysis to get the total gene population size, (i.e., 2739 genes for single cell analysis that had greater than 3 counts per cell in at least 10 cells and removing batch-effected genes for G0/G1 bulk RNA-sequencing).

Representation factors were calculated according to (Kim et al. 2001). The representation factor shows whether genes from one list (list A) are enriched in another list (list B), assuming that genes behave independently.

Statistics and Reproducibility

Data are presented as the mean or median ± standard deviation (SD) or standard error of the mean (SEM), as specified in the figure legends. Statistics were performed using GraphPad Prism 7.0 or analysis-specific functions in R. All statistical tests are specified in figure legends. The number of independent experiments is indicated in the figures, figure legends, or Methods.

REFERENCES

Anders S, Pyl PT, Huber W. 2015. HTSeq--a Python framework to work with high-throughput sequencing data. *Bioinformatics* **31**: 166-169.

Arora M, Moser J, Phadke H, Basha AA, Spencer SL. 2017. Endogenous Replication Stress in Mother Cells Leads to Quiescence of Daughter Cells. *Cell Rep* **19**: 1351-1364.

Artegiani B, Lyubimova A, Muraro M, van Es JH, van Oudenaarden A, Clevers H. 2017. A Single-Cell RNA Sequencing Study Reveals Cellular and Molecular Dynamics of the Hippocampal Neurogenic Niche. *Cell Rep* **21**: 3271-3284.

Bao S, Wu Q, McLendon RE, Hao Y, Shi Q, Hjelmeland AB, Dewhirst MW, Bigner DD, Rich JN. 2006. Glioma stem cells promote radioresistance by preferential activation of the DNA damage response. *Nature* **444**: 756-760.

Barr AR, Cooper S, Heldt FS, Butera F, Stoy H, Mansfeld J, Novak B, Bakal C. 2017. DNA damage during S-phase mediates the proliferation-quiescence decision in the subsequent G1 via p21 expression. *Nature communications* **8**: 14728.

Bergsland M, Werme M, Malewicz M, Perlmann T, Muhr J. 2006. The establishment of neuronal properties is controlled by Sox4 and Sox11. *Genes Dev* **20**: 3475-3486.

Bressan RB, Dewari PS, Kalantzaki M, Gangoso E, Matjusaitis M, Garcia-Diaz C, Blin C, Grant V, Bulstrode H, Gogolok S et al. 2017a. Efficient CRISPR/Cas9-assisted gene targeting enables rapid and precise genetic manipulation of mammalian neural stem cells. *Development* **144**: 635-648.

-. 2017b. Efficient CRISPR/Cas9-assisted gene targeting enables rapid and precise genetic manipulation of mammalian neural stem cells. *Development* **144**: 635-648.

Buettner F, Natarajan KN, Casale FP, Proserpio V, Scialdone A, Theis FJ, Teichmann SA, Marioni JC, Stegle O. 2015. Computational analysis of cell-to-cell

heterogeneity in single-cell RNA-sequencing data reveals hidden subpopulations of cells. *Nat Biotechnol* **33**: 155-160.

Chawla K, Tripathi S, Thommesen L, Laegreid A, Kuiper M. 2013. TFcheckpoint: a curated compendium of specific DNA-binding RNA polymerase II transcription factors. *Bioinformatics* **29**: 2519-2520.

Chen J, Li Y, Yu TS, McKay RM, Burns DK, Kernie SG, Parada LF. 2012a. A restricted cell population propagates glioblastoma growth after chemotherapy. *Nature* **488**: 522-526.

Chen J, McKay RM, Parada LF. 2012b. Malignant glioma: lessons from genomics, mouse models, and stem cells. *Cell* **149**: 36-47.

Choi KM, Kim JY, Kim Y. 2013. Distribution of the Immunoreactivity for Glycoprotein M6B in the Neurogenic Niche and Reactive Glia in the Injury Penumbra Following Traumatic Brain Injury in Mice. *Exp Neurobiol* **22**: 277-282.

Claus EB, Walsh KM, Wiencke JK, Molinaro AM, Wiemels JL, Schildkraut JM, Bondy ML, Berger M, Jenkins R, Wrensch M. 2015. Survival and low-grade glioma: the emergence of genetic information. *Neurosurg Focus* **38**: E6.

Coats S, Flanagan WM, Nourse J, Roberts JM. 1996. Requirement of p27Kip1 for restriction point control of the fibroblast cell cycle. *Science* **272**: 877-880.

Cordenonsi M, Zanconato F, Azzolin L, Forcato M, Rosato A, Frasson C, Inui M, Montagner M, Parenti AR, Poletti A et al. 2011. The Hippo transducer TAZ confers cancer stem cell-related traits on breast cancer cells. *Cell* **147**: 759-772.

Coronado D, Godet M, Bourillot PY, Tapponnier Y, Bernat A, Petit M, Afanassieff M, Markossian S, Malashicheva A, Iacone R et al. 2013. A short G1 phase is an intrinsic determinant of naive embryonic stem cell pluripotency. *Stem cell research* **10**: 118-131.

Danovi D, Folarin A, Gogolok S, Ender C, Elbatsh AM, Engstrom PG, Stricker SH, Gagrica S, Georgian A, Yu D et al. 2013. A high-content small molecule screen identifies sensitivity of glioblastoma stem cells to inhibition of polo-like kinase 1. *PLoS One* **8**: e77053.

Darmanis S, Sloan SA, Croote D, Mignardi M, Chernikova S, Samghababi P, Zhang Y, Neff N, Kowarsky M, Caneda C et al. 2017. Single-Cell RNA-Seq Analysis of Infiltrating Neoplastic Cells at the Migrating Front of Human Glioblastoma. *Cell Rep* **21**: 1399-1410.

Davis AA, Temple S. 1994. A self-renewing multipotential stem cell in embryonic rat cerebral cortex. *Nature* **372**: 263-266.

Ding Y, Herman JA, Toledo CM, Lang JM, Corrin P, Girard EJ, Basom R, Delrow JJ, Olson JM, Paddison PJ. 2017. ZNF131 suppresses centrosome fragmentation in glioblastoma stem-like cells through regulation of HAUS5. *Oncotarget*.

Ding Y, Hubert CG, Herman J, Corrin P, Toledo CM, Skutt-Kakaria K, Vazquez J, Basom R, Zhang B, Risler JK et al. 2013. Cancer-Specific requirement for BUB1B/BUBR1 in human brain tumor isolates and genetically transformed cells. *Cancer discovery* **3**: 198-211.

Dirks PB. 2008. Brain tumor stem cells: bringing order to the chaos of brain cancer. *J Clin Oncol* **26**: 2916-2924.

Doench JG, Fusi N, Sullender M, Hegde M, Vaimberg EW, Donovan KF, Smith I, Tothova Z, Wilen C, Orchard R et al. 2016. Optimized sgRNA design to maximize activity and minimize off-target effects of CRISPR-Cas9. *Nat Biotechnol* **34**: 184-191.

Doetsch F. 2003. A niche for adult neural stem cells. *Curr Opin Genet Dev* **13**: 543-550.

Fernandez-Calle R, Vicente-Rodriguez M, Gramage E, Pita J, Perez-Garcia C, Ferrer-Alcon M, Uribarri M, Ramos MP, Herradon G. 2017. Pleiotrophin regulates microglia-mediated neuroinflammation. *J Neuroinflammation* **14**: 46.

Filbin MG, Tirosh I, Hovestadt V, Shaw ML, Escalante LE, Mathewson ND, Neftel C, Frank N, Pelton K, Hebert CM et al. 2018. Developmental and oncogenic programs in H3K27M gliomas dissected by single-cell RNA-seq. *Science* **360**: 331-335.

Fischer M. 2017. Census and evaluation of p53 target genes. *Oncogene* **36**: 3943-3956.

Fujikawa A, Nagahira A, Sugawara H, Ishii K, Imajo S, Matsumoto M, Kuboyama K, Suzuki R, Tanga N, Noda M et al. 2016. Small-molecule inhibition of PTPRZ reduces tumor growth in a rat model of glioblastoma. *Scientific reports* **6**: 20473.

Fujikawa A, Sugawara H, Tanaka T, Matsumoto M, Kuboyama K, Suzuki R, Tanga N, Ogata A, Masumura M, Noda M. 2017. Targeting PTPRZ inhibits stem cell-like properties and tumorigenicity in glioblastoma cells. *Scientific reports* **7**: 5609.

Futreal PA, Coin L, Marshall M, Down T, Hubbard T, Wooster R, Rahman N, Stratton MR. 2004. A census of human cancer genes. *Nat Rev Cancer* **4**: 177-183.

Ginhoux F, Garel S. 2018. The mysterious origins of microglia. *Nat Neurosci* **21**: 897-899.

Hahn AT, Jones JT, Meyer T. 2009. Quantitative analysis of cell cycle phase durations and PC12 differentiation using fluorescent biosensors. *Cell cycle* **8**: 1044-1052.

Hoang-Minh LB, Siebzehnrubl FA, Yang C, Suzuki-Hatano S, Dajac K, Loche T, Andrews N, Schmoll Massari M, Patel J, Amin K et al. 2018. Infiltrative and drug-resistant slow-cycling cells support metabolic heterogeneity in glioblastoma. *EMBO J* **37**.

Hubert CG, Bradley RK, Ding Y, Toledo CM, Herman J, Skutt-Kakaria K, Girard EJ, Davison J, Berndt J, Corrin P et al. 2013. Genome-wide RNAi screens in human brain tumor isolates reveal a novel viability requirement for PHF5A. *Genes Dev* **27**: 1032-1045.

Ito A, Lai CH, Zhao X, Saito S, Hamilton MH, Appella E, Yao TP. 2001. p300/CBP-mediated p53 acetylation is commonly induced by p53-activating agents and inhibited by MDM2. *EMBO J* **20**: 1331-1340.

Johe KK, Hazel TG, Muller T, Dugich-Djordjevic MM, McKay RD. 1996. Single factors direct the differentiation of stem cells from the fetal and adult central nervous system. *Genes Dev* **10**: 3129-3140.

Johnson NL, Kemp AW, Kotz S. 2005. *Univariate discrete distributions*. Wiley, Hoboken, N.J.

Kamentsky L, Jones TR, Fraser A, Bray MA, Logan DJ, Madden KL, Ljosa V, Rueden C, Eliceiri KW, Carpenter AE. 2011. Improved structure, function and compatibility for CellProfiler: modular high-throughput image analysis software. *Bioinformatics* **27**: 1179-1180.

Kelly DP, Scarpulla RC. 2004. Transcriptional regulatory circuits controlling mitochondrial biogenesis and function. *Genes Dev* **18**: 357-368.

Kim J, Han D, Byun SH, Kwon M, Cho JY, Pleasure SJ, Yoon K. 2018. Ttyh1 regulates embryonic neural stem cell properties by enhancing the Notch signaling pathway. *EMBO Rep* **19**.

Kim SK, Lund J, Kiraly M, Duke K, Jiang M, Stuart JM, Eizinger A, Wylie BN, Davidson GS. 2001. A gene expression map for Caenorhabditis elegans. *Science* **293**: 2087-2092.

Kim SU, Park YH, Min JS, Sun HN, Han YH, Hua JM, Lee TH, Lee SR, Chang KT, Kang SW et al. 2013. Peroxiredoxin I is a ROS/p38 MAPK-dependent inducible antioxidant that regulates NF-kappaB-mediated iNOS induction and microglial activation. *J Neuroimmunol* **259**: 26-36.

Lan X, Jorg DJ, Cavalli FMG, Richards LM, Nguyen LV, Vanner RJ, Guilhamon P, Lee L, Kushida MM, Pellacani D et al. 2017. Fate mapping of human glioblastoma reveals an invariant stem cell hierarchy. *Nature* **549**: 227-232.

Langmead B, Trapnell C, Pop M, Salzberg SL. 2009. Ultrafast and memory-efficient alignment of short DNA sequences to the human genome. *Genome Biol* **10**: R25.

Lin H. 2008. Cell biology of stem cells: an enigma of asymmetry and self-renewal. *J Cell Biol* **180**: 257-260.

Lin JI, Poon CL, Harvey KF. 2013. The Hippo size control pathway--ever expanding. *Sci Signal* **6**: pe4.

Liu Y, Ye F, Yamada K, Tso JL, Zhang Y, Nguyen DH, Dong Q, Soto H, Choe J, Dembo A et al. 2011. Autocrine endothelin-3/endothelin receptor B signaling maintains cellular and molecular properties of glioblastoma stem cells. *Mol Cancer Res* **9**: 1668-1685.

Llorens-Bobadilla E, Zhao S, Baser A, Saiz-Castro G, Zwadlo K, Martin-Villalba A. 2015. Single-Cell Transcriptomics Reveals a Population of Dormant Neural Stem Cells that Become Activated upon Brain Injury. *Cell Stem Cell* **17**: 329-340.

Macosko EZ, Basu A, Satija R, Nemesh J, Shekhar K, Goldman M, Tirosh I, Bialas AR, Kamitaki N, Martersteck EM et al. 2015. Highly Parallel Genome-wide Expression Profiling of Individual Cells Using Nanoliter Droplets. *Cell* **161**: 1202-1214.

Mohrin M, Chen D. 2016. The mitochondrial metabolic checkpoint and aging of hematopoietic stem cells. *Curr Opin Hematol* **23**: 318-324.

Neftel C, Laffy J, Filbin MG, Hara T, Shore ME, Rahme GJ, Richman AR, Silverbush D, Shaw ML, Hebert CM et al. 2019. An Integrative Model of Cellular States, Plasticity, and Genetics for Glioblastoma. *Cell* **178**: 835-849 e821.

Nowakowski TJ, Bhaduri A, Pollen AA, Alvarado B, Mostajo-Radji MA, Di Lullo E, Haeussler M, Sandoval-Espinosa C, Liu SJ, Velmeshev D et al. 2017. Spatiotemporal gene expression trajectories reveal developmental hierarchies of the human cortex. *Science* **358**: 1318-1323.

Obernier K, Cebrian-Silla A, Thomson M, Parraguez JI, Anderson R, Guinto C, Rodas Rodriguez J, Garcia-Verdugo JM, Alvarez-Buylla A. 2018. Adult Neurogenesis Is Sustained by Symmetric Self-Renewal and Differentiation. *Cell Stem Cell* **22**: 221-234 e228.

Patel AP, Tirosh I, Trombetta JJ, Shalek AK, Gillespie SM, Wakimoto H, Cahill DP, Nahed BV, Curry WT, Martuza RL et al. 2014. Single-cell RNA-seq highlights intratumoral heterogeneity in primary glioblastoma. *Science* **344**: 1396-1401.

Plouffe SW, Meng Z, Lin KC, Lin B, Hong AW, Chun JV, Guan KL. 2016. Characterization of Hippo Pathway Components by Gene Inactivation. *Mol Cell* **64**: 993-1008.

Pollard SM, Conti L, Sun Y, Goffredo D, Smith A. 2006. Adherent neural stem (NS) cells from fetal and adult forebrain. *Cereb Cortex* **16 Suppl 1**: i112-120.

Pollard SM, Yoshikawa K, Clarke ID, Danovi D, Stricker S, Russell R, Bayani J, Head R, Lee M, Bernstein M et al. 2009. Glioma stem cell lines expanded in adherent culture have tumor-specific phenotypes and are suitable for chemical and genetic screens. *Cell Stem Cell* **4**: 568-580.

Puram SV, Tirosh I, Parikh AS, Patel AP, Yizhak K, Gillespie S, Rodman C, Luo CL, Mroz EA, Emerick KS et al. 2017. Single-Cell Transcriptomic Analysis of Primary and Metastatic Tumor Ecosystems in Head and Neck Cancer. *Cell* **171**: 1611-1624 e1624.

Reya T, Morrison SJ, Clarke MF, Weissman IL. 2001. Stem cells, cancer, and cancer stem cells. *Nature* **414**: 105-111.

Robinson MD, McCarthy DJ, Smyth GK. 2010. edgeR: a Bioconductor package for differential expression analysis of digital gene expression data. *Bioinformatics* **26**: 139-140.

Roche B, Arcangioli B, Martienssen R. 2017. Transcriptional reprogramming in cellular quiescence. *RNA Biol* **14**: 843-853.

Sakamoto M, Hirata H, Ohtsuka T, Bessho Y, Kageyama R. 2003. The basic helix-loop-helix genes Hesr1/Hey1 and Hesr2/Hey2 regulate maintenance of neural precursor cells in the brain. *J Biol Chem* **278**: 44808-44815.

Sakaue-Sawano A, Kurokawa H, Morimura T, Hanyu A, Hama H, Osawa H, Kashiwagi S, Fukami K, Miyata T, Miyoshi H et al. 2008. Visualizing spatiotemporal dynamics of multicellular cell-cycle progression. *Cell* **132**: 487-498.

Sanjana NE, Shalem O, Zhang F. 2014. Improved vectors and genome-wide libraries for CRISPR screening. *Nat Methods* **11**: 783-784.

Santos A, Wernersson R, Jensen LJ. 2015. Cyclebase 3.0: a multi-organism database on cell-cycle regulation and phenotypes. *Nucleic Acids Res* **43**: D1140-1144.

Scott CE, Wynn SL, Sesay A, Cruz C, Cheung M, Gomez Gaviro MV, Booth S, Gao B, Cheah KS, Lovell-Badge R et al. 2010. SOX9 induces and maintains neural stem cells. *Nat Neurosci* **13**: 1181-1189.

Shalem O, Sanjana NE, Hartenian E, Shi X, Scott DA, Mikkelsen TS, Heckl D, Ebert BL, Root DE, Doench JG et al. 2014. Genome-scale CRISPR-Cas9 knockout screening in human cells. *Science* **343**: 84-87.

Sherr CJ. 1995. D-type cyclins. *Trends in biochemical sciences* **20**: 187-190.

Sherr CJ, McCormick F. 2002a. The RB and p53 pathways in cancer. *Cancer Cell* **2**: 103-112.

-. 2002b. The RB and p53 pathways in cancer. *Cancer Cell* **2**: 103-112.

Spencer SL, Cappell SD, Tsai FC, Overton KW, Wang CL, Meyer T. 2013. The proliferation-quiescence decision is controlled by a bifurcation in CDK2 activity at mitotic exit. *Cell* **155**: 369-383.

Stupp R, Mason WP, van den Bent MJ, Weller M, Fisher B, Taphoorn MJ, Belanger K, Brandes AA, Marosi C, Bogdahn U et al. 2005. Radiotherapy plus concomitant and adjuvant temozolomide for glioblastoma. *N Engl J Med* **352**: 987-996.

Sun Y, Pollard S, Conti L, Toselli M, Biella G, Parkin G, Willatt L, Falk A, Cattaneo E, Smith A. 2008. Long-term tripotent differentiation capacity of human neural stem (NS) cells in adherent culture. *Mol Cell Neurosci* **38**: 245-258.

Susaki E, Nakayama K, Nakayama KI. 2007. Cyclin D2 translocates p27 out of the nucleus and promotes its degradation at the G0-G1 transition. *Mol Cell Biol* **27**: 4626-4640.

Szklarczyk D, Morris JH, Cook H, Kuhn M, Wyder S, Simonovic M, Santos A, Doncheva NT, Roth A, Bork P et al. 2017. The STRING database in 2017: quality-controlled protein-protein association networks, made broadly accessible. *Nucleic Acids Res* **45**: D362-D368.

TCGA. 2008. Comprehensive genomic characterization defines human glioblastoma genes and core pathways. *Nature* **455**: 1061-1068.

Than-Trong E, Ortica-Gatti S, Mella S, Nepal C, Alunni A, Bally-Cuif L. 2018. Neural stem cell quiescence and stemness are molecularly distinct outputs of the Notch3 signalling cascade in the vertebrate adult brain. *Development* **145**.

Tirosh I, Venteicher AS, Hebert C, Escalante LE, Patel AP, Yizhak K, Fisher JM, Rodman C, Mount C, Filbin MG et al. 2016. Single-cell RNA-seq supports a developmental hierarchy in human oligodendroglioma. *Nature* **539**: 309-313.

Toledo CM, Ding Y, Hoellerbauer P, Davis RJ, Basom R, Girard EJ, Lee E, Corrin P, Hart T, Bolouri H et al. 2015. Genome-wide CRISPR-Cas9 Screens Reveal Loss of Redundancy between PKMYT1 and WEE1 in Glioblastoma Stem-like Cells. *Cell Rep* **13**: 2425-2439.

Toledo CM, Herman JA, Olsen JB, Ding Y, Corrin P, Girard EJ, Olson JM, Emili A, DeLuca JG, Paddison PJ. 2014. BuGZ is required for Bub3 stability, Bub1 kinetochore function, and chromosome alignment. *Dev Cell* **28**: 282-294.

Trapnell C, Roberts A, Goff L, Pertea G, Kim D, Kelley DR, Pimentel H, Salzberg SL, Rinn JL, Pachter L. 2012. Differential gene and transcript expression analysis of RNA-seq experiments with TopHat and Cufflinks. *Nat Protoc* **7**: 562-578.

Tripathi V, Shen Z, Chakraborty A, Giri S, Freier SM, Wu X, Zhang Y, Gorospe M, Prasanth SG, Lal A et al. 2013. Long noncoding RNA MALAT1 controls cell cycle

progression by regulating the expression of oncogenic transcription factor B-MYB. *PLoS Genet* **9**: e1003368.

Venteicher AS, Tirosh I, Hebert C, Yizhak K, Neftel C, Filbin MG, Hovestadt V, Escalante LE, Shaw ML, Rodman C et al. 2017. Decoupling genetics, lineages, and microenvironment in IDH-mutant gliomas by single-cell RNA-seq. *Science* **355**: eaai8478.

Weinberg RA. 1995. The retinoblastoma protein and cell cycle control. *Cell* **81**: 323-330.

Wilson KE, Li YW, Yang N, Shen H, Orillion AR, Zhang J. 2014. PTPN14 forms a complex with Kibra and LATS1 proteins and negatively regulates the YAP oncogenic function. *J Biol Chem* **289**: 23693-23700.

Wu HN, Cao XL, Fang Z, Zhang YF, Han WJ, Yue KY, Cao Y, Zheng MH, Wang LL, Han H. 2019. Deficiency of Ttyh1 downstream to Notch signaling results in precocious differentiation of neural stem cells. *Biochem Biophys Res Commun* **514**: 842-847.

Xu W, Yang H, Liu Y, Yang Y, Wang P, Kim SH, Ito S, Yang C, Wang P, Xiao MT et al. 2011. Oncometabolite 2-hydroxyglutarate is a competitive inhibitor of alpha-ketoglutarate-dependent dioxygenases. *Cancer Cell* **19**: 17-30.

Yan H, Parsons DW, Jin G, McLendon R, Rasheed BA, Yuan W, Kos I, Batinic-Haberle I, Jones S, Riggins GJ et al. 2009. IDH1 and IDH2 mutations in gliomas. *N Engl J Med* **360**: 765-773.

Yao G, Lee TJ, Mori S, Nevins JR, You L. 2008. A bistable Rb-E2F switch underlies the restriction point. *Nat Cell Biol* **10**: 476-482.

Young MD, Wakefield MJ, Smyth GK, Oshlack A. 2010. Gene ontology analysis for RNA-seq: accounting for selection bias. *Genome Biol* **11**: R14.

Yu G, He QY. 2016. ReactomePA: an R/Bioconductor package for reactome pathway analysis and visualization. *Mol Biosyst* **12**: 477-479.

Zetterberg A, Larsson O, Wiman KG. 1995. What is the restriction point? *Curr Opin Cell Biol* **7**: 835-842.

Zhang L, Laaniste L, Jiang Y, Alafuzoff I, Uhrbom L, Dimberg A. 2016. Pleiotrophin enhances PDGFB-induced gliomagenesis through increased proliferation of neural progenitor cells. *Oncotarget* **7**: 80382-80390.

Zhang N, Bai H, David KK, Dong J, Zheng Y, Cai J, Giovannini M, Liu P, Anders RA, Pan D. 2010. The Merlin/NF2 tumor suppressor functions through the YAP oncoprotein to regulate tissue homeostasis in mammals. *Dev Cell* **19**: 27-38.

Zheng GX, Terry JM, Belgrader P, Ryvkin P, Bent ZW, Wilson R, Ziraldo SB, Wheeler TD, McDermott GP, Zhu J et al. 2017. Massively parallel digital transcriptional profiling of single cells. *Nature communications* **8**: 14049.

Zong H, Parada LF, Baker SJ. 2015. Cell of origin for malignant gliomas and its implication in therapeutic development. *Cold Spring Harbor perspectives in biology* **7**.

Acknowledgements

We thank Jon Cooper, Eric Holland, and members of the Paddison lab for helpful discussions, and Atsushi Miyawaki and Sabrina Spencer for providing reagents. This work was supported by the following grants: Interdisciplinary Training in Cancer Fellowship NCI T32CA080416 (PH), NCI/NIH (R01CA190957; R21CA170722; P30CA15704) (PP), DoD Translational New Investigator Award CA100735 (PP), and the Pew Biomedical Scholars Program (PP).

Author contributions

Project conception and design was carried out by P.J.P., C.L.P., H.M.F., and C.M.T. CRISPR-Cas9 screening was performed by H.M.F., C.M.T., and P.H.; hit validation was performed by H.M.F, C.M.T., P.H., and M.K.; critical reagents were generated by P.C. and L.C.; screen and RNA-seq data analysis and statistics was performed by S.A. with input from A.P.; scRNA-seq was performed by H.M.F. under supervision of J.L.M.-F. and C.T., and analyzed by C.L.P.; H.B. performed cancer mutation analysis; J.M. designed the tiling library; S.M.P. provided and validated the hNSCs; and P.J.P. , H.M.F., A.P., and C.L.P. wrote the manuscript with input from all authors.

Competing interests

The authors declare no competing interests.

Fig. 1: Gene Expression Map of Cell Cycle and Candidate G0 and G1 Subpopulations using Single Cell RNA-seq in hNSCs

A, Overview of the selection scheme used for isolating G0/G1-enriched and bulk cultured hNSCs for scRNA-seq.

B, Transcriptional clusters of unsorted U5-NSCs derived through an unbiased shared nearest neighbor (SNN) modularity and visualized through a t-Distributed Stochastic Neighbor Embedding (tSNE) comparison.

C, Proportion of cells found in each cluster for the WT U5-NSCs.

D, Network derived from Canberra distance measures shows connections between the cell cycle clusters.

E, Heat map of the relative expression (row-wise z-score) for the top 10 non-redundant genes for each prominent cluster in WT U5-NSCs and gene ontology analysis of the up-regulated genes defining each cluster. BP = biological process; R = Reactome; MF = molecular function; CC = cellular component; n/a = non-applicable (gene list derived in this paper). Featured gene ontology groups selected based on significance (p-adj.<.01), representation, and/or non-redundancy. Full cluster-defining gene list is in Supplemental Table S1 and full gene ontology and reactome analysis is in Supplemental Table S2.

Figure 1

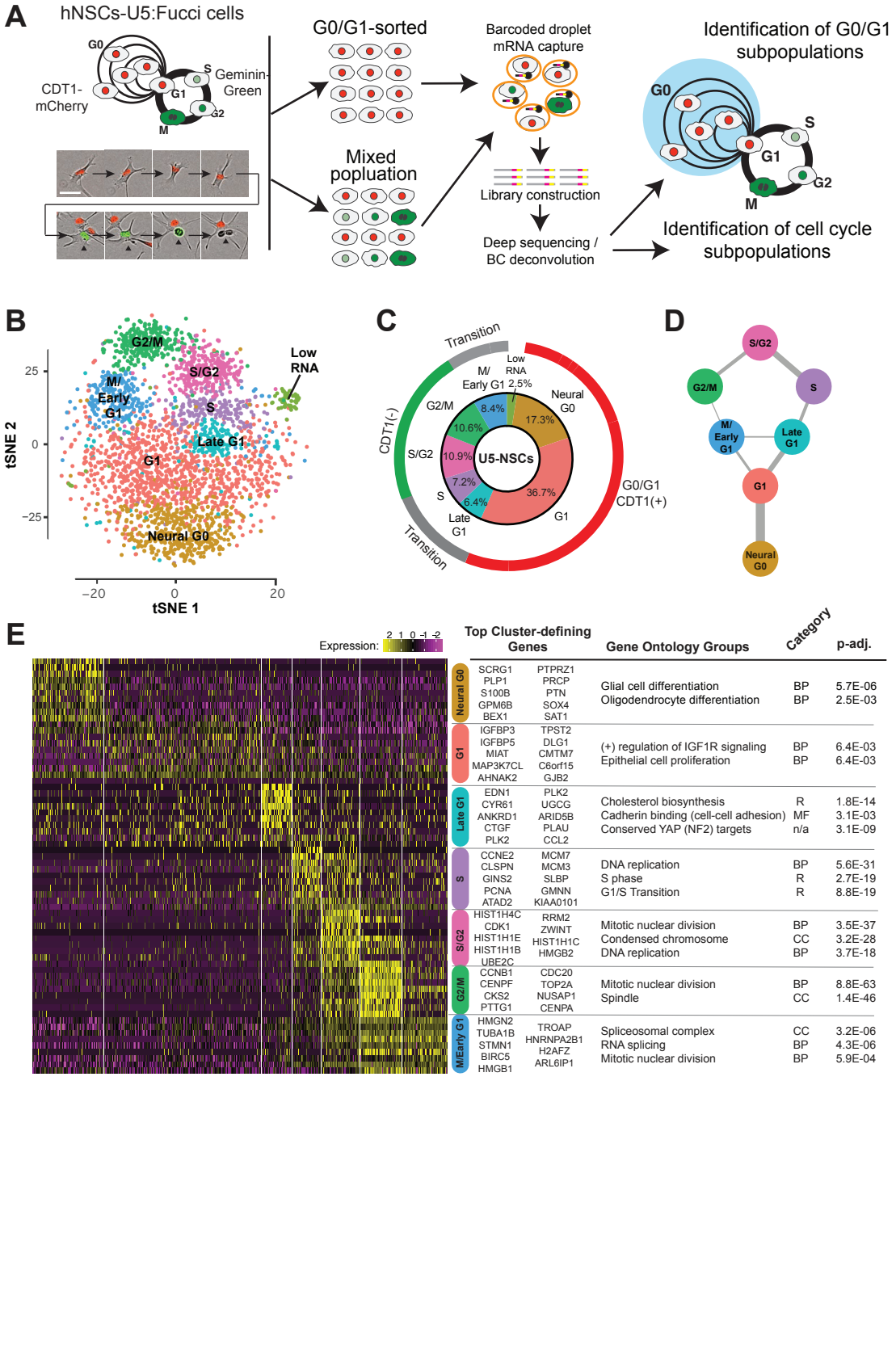

Fig. 2: Comparison of hNSC cell cycle classifier with other neuroepithelial-derived cell populations.

A, Model of the cell cycle of cultured hNSCs based on single cell transcriptomes.

B, Overlap of the Neural G0 cluster with single cell transcriptomic profiles of quiescent neural stem cells (qNSCs) and activated (aNSC) NSCs/neural progenitors from adult rodent hippocampal niche(Llorens-Bobadilla et al. 2015; Artegiani et al. 2017). Significance assessed using hypergeometric analysis. OPC = oligodendrocyte progenitor.

C, D, Significance of overlap of the neurogenesis cell subpopulation-defining genes in the early neurogenic lineage from two murine single cell RNA-sequencing studies compared to single cell cluster definitions (up-regulated genes) from unsorted U5-hNSCs grown in culture. Clusters presented in order of increasing activation with quiescent neural stem cells on the left and proliferating progenitors on the right. Significance assessed though hypergeometric analysis. RF = representation factor.

E, Application of the hNSCs cell cycle classifier to scRNA-seq data from the developing human telencephalon (from (Nowakowski et al. 2017)). RG = radial glia, div = dividing. All cell type abbreviations are available in Table S3. Red asterisks indicate cells derived from the excitatory cortical neuron lineage, which originate from radial glial cells. Blue asterisks indicate cells from inhibitory cortical interneuron lineage.

Figure 2

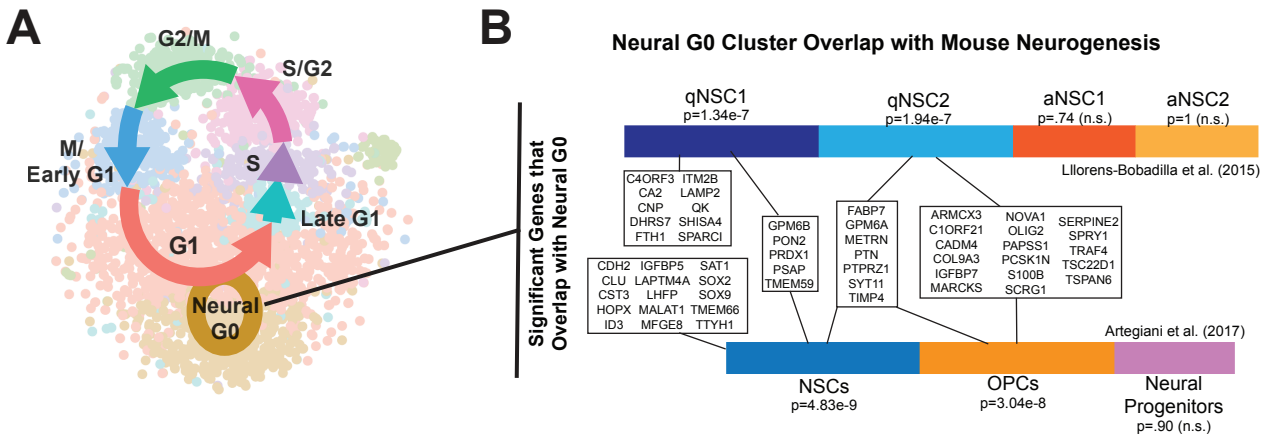

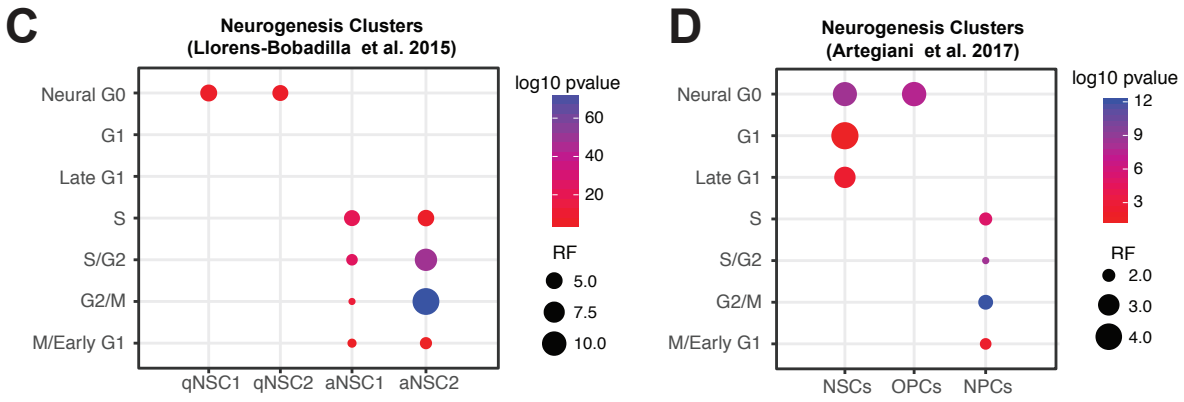

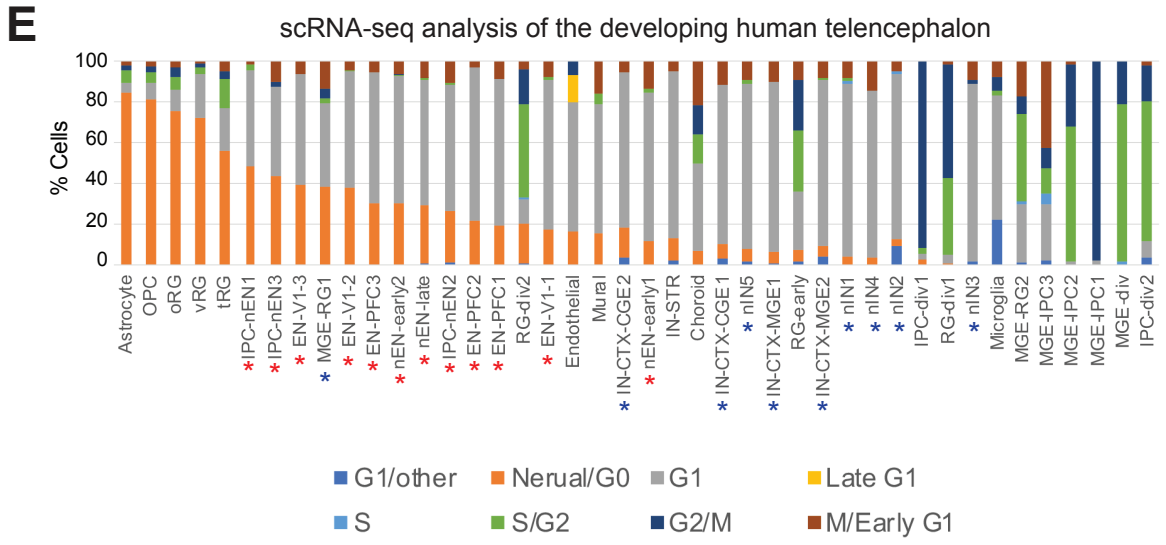

Table 1

Data set	Tumor Type	# tumors	G1/other	Neural G0	G1	S	S/G2	G2/M	# cells
GSE70630	**II IDH1^{mut}-O**	**6**	**<0.1**	**95.5**	**2.6**	**0.1**	**1.0**	**0.6**	**4112**
	CL		0	95.7	2.7	<0.1	0.9	0.4	1208
	MS		0.2	93.5	4.7	0.1	0.4	0.3	933
	PN		0	96.3	1.5	0.2	1.3	0.7	1971
GSE89567	**III IDH1^{mut}-A**	**7**	**0.9**	**76.0**	**16.4**	**0.2**	**1.6**	**1.5**	**6341**
	CL		<0.1	89.8	4.3	0.2	2.3	2.7	1595
	MS		3.3	28.5	55.8	0	0.3	0.4	1599
	PN		0	93.2	2.5	0.4	1.9	1.5	3147
GSE84465	**IV IDH^{wt}**	**4**	**13.1**	**31.1**	**52.5**	**0.6**	**1.2**	**0.9**	**1029**
	CL		7.2	38.7	51.4	0.6	0.7	1.1	706
	MS		35.5	2.4	59.7	0	0	0	124
	PN		20.1	22.1	51.8	1.0	3.5	0.5	199
GSE57872	**IV IDH^{wt}**	**6**	**1.7**	**34.2**	**56.3**	**0.5**	**5.7**	**1.2**	**403**
	CL		0.7	48.9	42.2	0.7	6.7	0.7	135
	MS		3.9	13.2	81.6	0	1.3	0	152
	PN		0	43.1	41.4	0.9	10.3	3.4	116
GSE131928	**IV IDH^{wt}**	**31**	**12.4**	**39.0**	**30.9**	**0.1**	**4.8**	**7.7**	**24131**
	CL		0.1	14.5	5.8	0.1	2.1	3.6	6512
	MS		7.5	5.9	19.8	0.1	0.7	1.1	9143
	PN		4.7	18.5	5.3	0.2	2.1	3.0	8475
GSE102130	**DMG H3K27M**	**6**	**0.7**	**73.4**	**16.5**	**1.6**	**4**	**3.1**	**2458**
	CL		0	79.0	14.3	0.3	1.8	3.3	391
	MS		0.9	66.7	20.9	0.2	3.5	3	541
	PN		0	69.6	9.8	0.9	10.0	8.1	1526
GSE103322	**HNSCC**	**21**	**2.5**	**0**	**80.3**	**6.6**	**2.1**	**9.9**	**2161**

Table I: Percentage of glioma tumor cells defined by hNSCs cell cycle classifier. O = oligodendroglioma; A = astrocytoma; DMG = Diffuse midline glioma; HNSCC = head and neck squamous cell carcinoma; CL = classical subtype; MS = mesenchymal subtype; PN = proneural subtype.

Fig. 3: Neural G0 gene expression in 641 human gliomas.

A, Relative Neural G0 eigengene expression between grade II, III, and IV tumors (TCGA; LGG and GBM). An eigengene represents the common variation across each patient tumor for the Neural G0 genes, i.e. first principal component corrected for direction if necessary. All pairwise Student's t-tests comparisons had p-values <0.003.

B, Comparison of cell cycle and Neural G0 eigengene expression in each glioma. Each tumor is colored by its grade (green = II, red = III, and purple = IV).

C, Differences in the distribution of tumor grade between tumors with top 25% and bottom 25% of Neural G0 eigengene expression.

D, Kaplan Meier survival plot of tumors with top 25% and bottom 25% of Neural G0 eigengene expression of Neural G0 genes. A Fleming-Harrington survival p-value was used to determine significance.

Figure 3

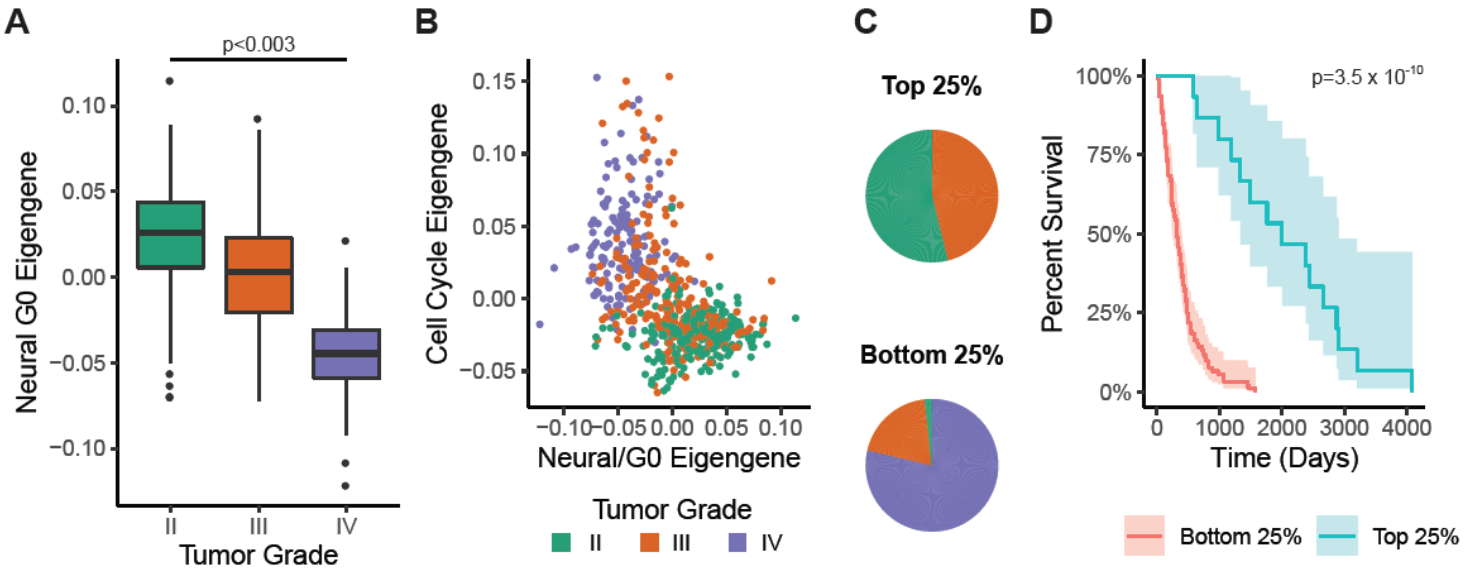

Fig. 4: CRISPR-Cas9 gene knockout screens to identify candidate Neural G0 regulating genes in hNSCs.

A, Schematic of CRISPR-Cas9 knockout screen design.

B, Enrichment of guide DNA following 21 days outgrowth post-selection using GECKO library (n=2). Colored guides are enriched (z-score>2; green) or depleted (z-score<2; red) with false discovery rate (FDR<0.05). Statistical source data provided in Supplementary Table S6.

C, Overlap of screen hits between the four CRISPR-Cas9 screens. For all screens, hits were defined as genes having multiple guides with FDR<.01 and z-score >2. For Brunello library, there were additional requirements of at least one guide with z-score >3 and at least 20 reads at Day 0. *CREBBP*, *NF2*, *PTPN14*, *TAOK1*, and *TP53* were defined as hits in every screen.

D, Flow analysis of U5-NSC:GFP with LV-sgRNA:Cas9 retest pools competing with wild-type (WT) U5-NSC over a 23 day outgrowth with ~10% initial proportion (n=3). Competition index refers to the relative increase in %GFP+ compared with initial proportion and mean sgNTC.

E, Doubling time measurements (>14 days post-selection) in U5-NSCs or GSCs after 3-5 days outgrowth. n≥3, as noted in bars for each guide. The data are presented as the mean ± standard deviation (SD). Significance was assessed using a two-tailed student's t-test.

Figure 4

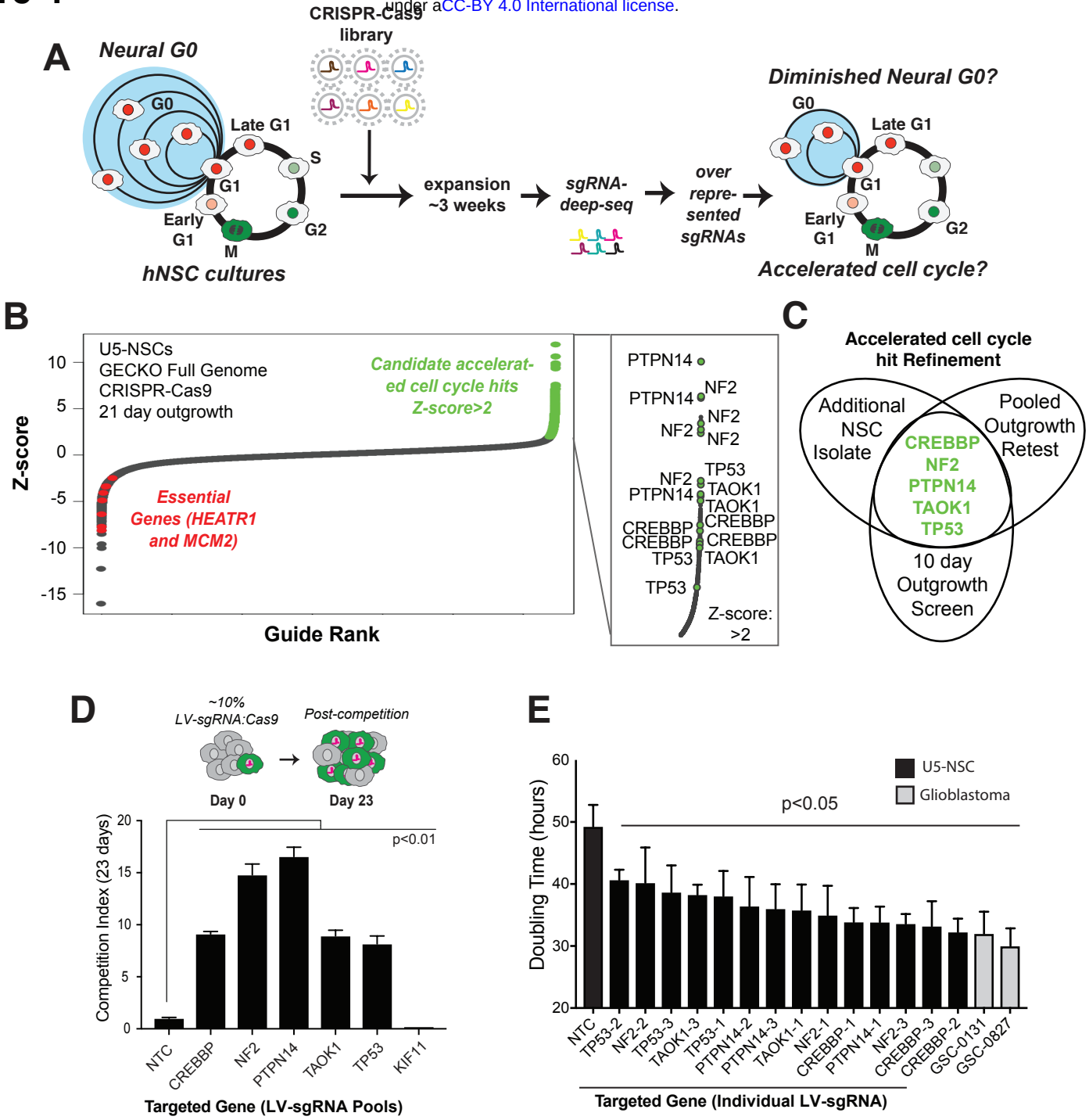

Fig. 5: Reduction of G0/G1 Transit Time in NSCs after KO of *CREBBP*, *NF2*, *PTPN14*, *TAOK1*, or *TP53*

A, Representative contour plot of flow cytometry for Fucci (Sakaue-Sawano et al. 2008) in U5-NSCs after targeting of a non-growth limiting (NGL) control gene, *GNAS1*. Values are similar to wild-type and NTC U5-NSCs under similar culture conditions. The system relies on cell-cycle dependent degradation of fluorophores using the degrons from CDT1 *(*amino acids (aa) 30-120) (present in G0 and G1; mCherry) and geminin (aa1-110) (present in S, G2, and M; monomeric Azami-Green (mAG)).

B, Representative contour maps of flow cytometry for Fucci following loss of *NF2*, *PTPN14*, *TAOK1*, *CREBBP*, and *TP53*.

C, Ratio of G0/G1 (mCherry-CDT1+) to S/G2/M (mAG-Geminin+) from (A) and (B). Values are mean from 4 individually-tested LV guides per gene at 21 days post-selection.

D, G0/G1 and S/G2/M transit times using time-lapse microscopy and Fucci. Differences in G0/G1 are statistically significant with $p<0.0001$ for targeted U5-NSCs and $p=0.0006$ for GSC-131 compared to NTC.

The data are presented as the mean ± SD. Significance was assessed using a two-tailed student's t-test (**C**) or Mann-Whitney test (**D**).

Figure 5

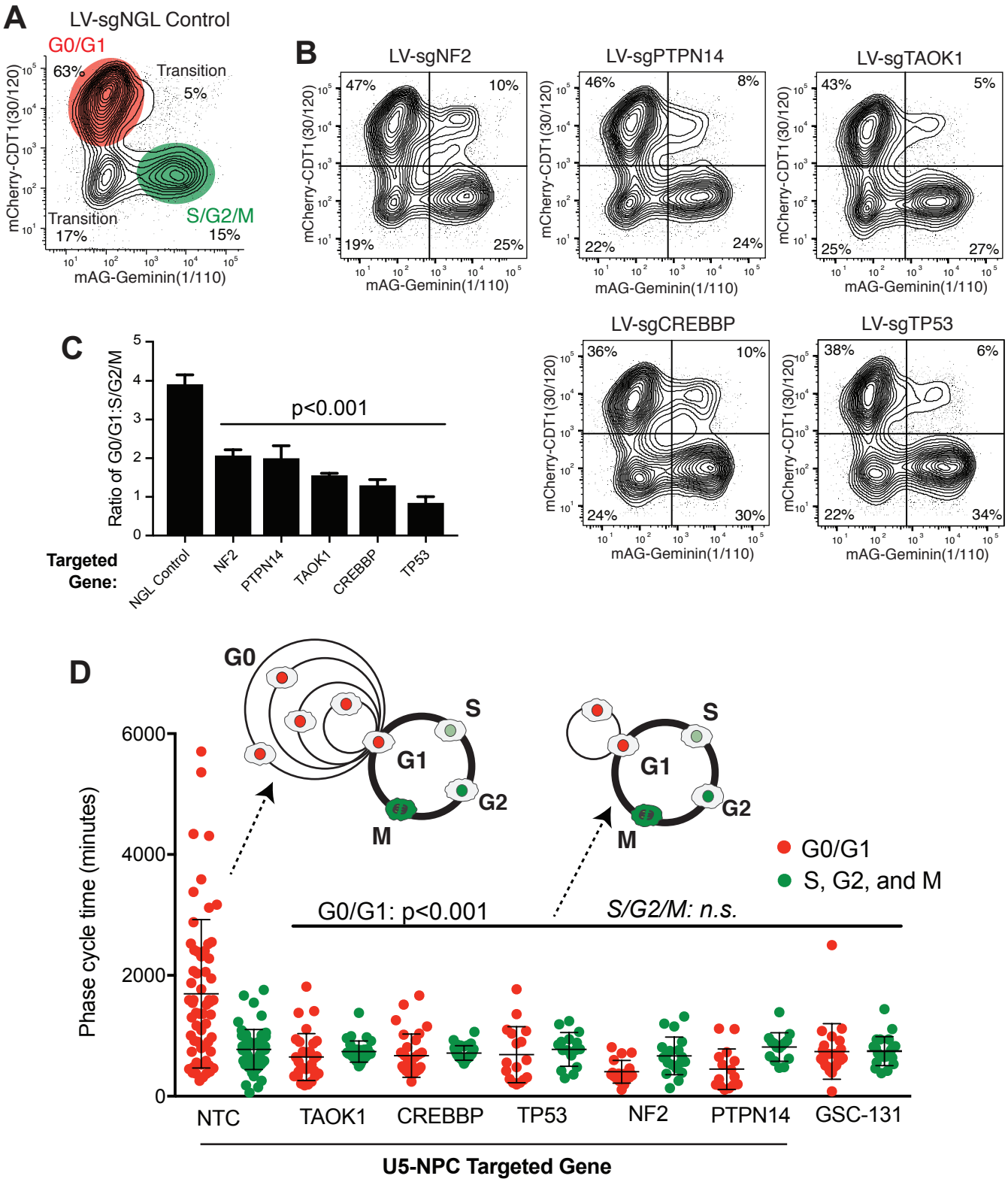

Fig. 6: Transcriptional Reprogramming of G0/G1 Following Loss of G0-skip Genes

A, Schematic of G0/G1 sorting for gene expression analysis: mCherry-CDT1+ U5-NSCs (red box), heat maps of the significantly altered genes (FDR<0.05) between WT unsorted U5-NSCs and NTC and WT G0/G1 U5-NSCs, and gene ontology analysis (Young et al. 2010) of some of the top biological processes down-regulated and reactome groups (Yu and He 2016) up-regulated in the G0/G1 sorted cells. Full list in Supplementary Tables S10 & S11.

B, Dendrogram of unbiased hierarchical clustering of gene expression from G0/G1-sorted U5-NSCs with the number genes up (green) and down (red) regulated (FDR<0.05) in each KO compared to NTC. Complete results in Supplementary Table S10.

C, Heat map of $\log_2$FC compared to NTC for key genes changed in G0/G1 in following loss of *TP53, NF2/PTPN14*, *TAOK1*, and/or *CREBBP*, including genes from TP53 targets, YAP targets, the cell cycle, Hippo signaling, and electron transport genes. White dots indicate FDR<0.05.

D-E, Significance of overlap of the down (D) and up (E) regulated genes from bulk RNA-sequencing of G0/G1 sorted cells with the single cell cluster definitions (up-regulated genes). Significance assessed though hypergeometric analysis. RF = representation factor.

Figure 6